www.sciencemag.org/cgi/content/full/337/6098/1075/DC1

Supplementary Materials for

Biogenic Potassium Salt Particles as Seeds for Secondary Organic Aerosol in the Amazon

Christopher Pöhlker,[1]* Kenia T. Wiedemann,[2,3,4] Bärbel Sinha,[5,6] Manabu Shiraiwa,[1,7] Sachin S. Gunthe,[1,8] Mackenzie Smith,[3] Hang Su,[1] Paulo Artaxo,[2] Qi Chen,[3] Yafang Cheng,[1] Wolfgang Elbert,[1] Mary K. Gilles,[9] Arthur L. D. Kilcoyne,[10] Ryan C. Moffet,[8,11] Markus Weigand,[12] Scot T. Martin,[3] Ulrich Pöschl,[1]* Meinrat O. Andreae[1]

*To whom correspondence should be addressed. E-mail: c.pohlker@mpic.de (C.P.); u.poschl@mpic.de (U.P.)

Published 31 August 2012, *Science* **337**, 1075 (2012)
DOI: 10.1126/science.1123264

This PDF file includes:

Materials and Methods
Supplementary Text
Figs. S1 to S12
Tables S1 to S9
References

S1 Materials and Methods

S1.1 Aerosol sampling

Aerosol samples were collected with a single stage impactor (*35*) on silicon nitride substrates (Si_3N_4, membrane width 0.5 mm, membrane thickness 100 nm, Silson Ltd, Northampton, UK). The volumetric flow through the impactor was 1-1.5 l min^{-1}, corresponding to a nominal cut-off in the range of 0.5-0.8 µm. On the Si_3N_4 substrate the majority of particles larger than 1 µm was concentrated in a central impaction spot, whereas smaller particles (down to 0.1 µm) were collected via diffusive deposition around this spot. Regions of diffusive deposition have been chosen for STXM analysis because of the relatively high abundance of small particles and appropriate particle coverage. The samples were collected 2-2.5 m above ground level. Sampling times between 30 to 60 min ensured appropriate particle coverage on the substrates. The samples were sealed in air-tight containers, and stored at 4°C and 20-30 % relative humidity (RH) in the dark. STXM-NEXAFS analysis was done three weeks, and NanoSIMS and SEM analysis four weeks after collection. Several individual particles were investigated with two STXM instruments (ALS-STXM 5.3.2.2 in Berkeley and four months later at the MAXYMUS-STXM in Berlin, Sect. S1.5). The measurements with the two STXM instruments yielded very similar NEXAFS spectra for the investigated Amazonian SOA samples, and the quantitative analysis gave consistent results.

S1.2 Amazonian aerosols and sampling locations

The samples for this study were collected during the wet season on 13 and 14 May 2011 at a very remote site 150 km NE of the city of Manaus, Brazil, in an untouched forest area (Amazonian Tall Tower Observatory (ATTO) site, 2.14336° S, 59.00056° W, 120 m above sea level) (Table S1). The sampled air masses came mainly from the northeast across ~1000 km of untouched forest areas. Nine-day back trajectories indicated the arrival of air masses from northeastern directions, originating over the Atlantic Ocean in the direction of Cape Verde. Figure S1 shows back trajectories and the cumulative rainfall during this time, which indicates strong wet deposition, and therefore dominance of local and regional aerosol sources. In addition, no soot or other combustion released particles were found in STXM-NEXAFS, SEM, and NanoSIMS analyses. NEXAFS spectra are particularly sensitive to soot and other combustion derived particles that contain a significant amount of aromatic moieties, and therefore, exhibit

strong spectral features at 285 eV (*36-38*). Hence, the samples are thought to be free of anthropogenic influences such as biomass burning in the Amazon (*19-20*) and long-range transport of biomass burning emissions from Africa.

An earlier set of samples had been collected on 15 May 2010 at a remote site 60 km NNW of Manaus in Brazil (ZF2 site, 2.59454° S, 60.20929° W, 90 m above sea level) (Table S1). Previously, this site (with K34 and TT34 towers) has been used for field measurement campaigns such as AMAZE-08 (*6-7, 34, 39*), whereas the ATTO site was established recently (2011). While this study is focused on the samples from the pristine ATTO site, the measurements from the ZF2 samples have been added as independent confirmation for the size dependence of the potassium mass fraction in organic aerosol particles (Fig. 3).

S1.3 Laboratory generated SOA from the Harvard Environmental Chamber

The Harvard Environmental Chamber (*40*) was operated under continuous flow conditions to generate particles composed of secondary organic material with ammonium sulfate seeds. For all experiments, the chamber relative humidity was 40 %, the temperature was 25°C, and ammonium sulfate seed particles were injected. The secondary organic material samples were produced by photooxidation of isoprene, dark ozonolysis of α-pinene, and dark ozonolysis of β-caryophyllene. The oxygen-to-carbon ratio (O:C) and mass loading of the secondary organic material in the chamber outflow was characterized by an Aerodyne high-resolution time-of-flight aerosol mass spectrometer (HR-ToF-AMS) (*41*). The recent updates of Chen et al. (*42*) were applied in the analysis of O:C. A summary of the experimental conditions can be found in Table S2.

The α-pinene and β-caryophyllene ozonolysis experiments largely followed the procedures detailed in Shilling et al. (*43*) and Chen et al. (*44*), respectively. Briefly, a solution of α-pinene in 2-butanol or β-caryophyllene in cyclohexane was continually injected into a gently warmed glass bulb using a syringe pump. The solution evaporated in a pure air flow and was swept into the chamber. Ozone was generated outside the chamber by passing a pure air flow around an ultraviolet light and the resulting flow was injected into the chamber. Within the chamber, the reaction of α-pinene or β-caryophyllene with ozone formed secondary products, and those of sufficiently low volatility condensed onto the surfaces of the crystalline seed particles.

The generation of isoprene secondary organic material generally followed the method described in King et al. (*45*). One alteration was that for these experiments the ammonium sulfate seed particles were deliquesced aqueous droplets. Gas-phase isoprene and hydrogen peroxide (H_2O_2) were injected into the chamber, and isoprene reacted with the OH radicals produced by the photolysis of H_2O_2 by irradiation in the chamber. Some of the products of this reaction were of low volatility and partitioned to the seed particles. The laboratory-generated SOA was collected by impaction sampling on silicon nitride substrates using a single stage impactor (see. Sect. S1.1).

S1.4 Reference aerosols from pure organic compounds

The following chemicals, purchased from Sigma Aldrich, were used as reference standards: serine, aspartic acid, bovine serum albumin (BSA), glucose, and glucosamine·HCl. Chemicals were used without further purification and dissolved in deionized water (Millipore - Milli Q plus 185, 18.2 MΩ cm). Reference aerosol was generated by spray-drying of the pure organic compounds in aqueous solution (1 mmol l^{-1}) using a constant output atomizer operated with filtered particle-free pressurized air (250 kPa, 3 lpm). The polydisperse aerosol flow was dried to a relative humidity of <15 % (silica-gel diffusion dryer). Further, the generated aerosols were passed through a radioactive neutralizer (Kr^{85}, 74 MBq or 2 mCi) to generate charge equilibrium, and then to a differential mobility analyzer (DMA; TSI 3080 electrostatic classifier). This facilitated the selection of particles of suitable size for further analysis (0.35-0.6 µm). The output from this DMA was split in two for aerosol sampling (1 lpm) and for a condensation particle counter (TSI 3786, 0.6 lpm) to monitor particle concentration. The reference aerosols were collected by: (i) impaction sampling on Si_3N_4 substrates using a single stage impactor (see. Sect. S1.1) and (ii) electrostatic precipitation on TEM grids (300-mesh copper mesh, 10-15 nm carbon coating, Plano GmbH, Wetzlar, DE) using an electrostatic sampler (*46*). The STXM analysis of reference samples on both substrates yielded particle diameters in the expected size range, indicating that no particle fragmentation occurred in the course of sampling (i.e. impaction on Si_3N_4 membranes).

S1.5 STXM-NEXAFS measurements and data processing

STXM-NEXAFS analysis was conducted at the Lawrence Berkeley National Laboratory Advanced Light Source (LBNL ALS), Berkeley, CA, USA, at beamline 5.3.2.2 and at the MAXYMUS beamline (UE46_PGM-2) at BESSY II, Helmholtz-Zentrum, Berlin, Germany.

The ALS-STXM instrument is located at the bending magnet beamline 5.3.2.2 at the ALS electron storage ring (1.9 GeV, 500 mA stored current in top-off mode) and provides a photon flux of ~10^7 s^{-1} in the soft X-ray region (250-800 eV). It is equipped with a spherical grating monochromator (resolving power $E/\Delta E \leq 5000$), a Fresnel zone plate with 25 nm spatial resolution and a phosphor coated Lucite tube coupled with a photomultiplier. Samples are analyzed in a He-filled chamber (~30 kPa). The accessible energy range (250-800 eV) includes the carbon K-absorption edge (283.8 eV), the potassium $L_{3,2}$-edge (294.6 eV), the calcium $L_{3,2}$-edge (349.3 eV), the nitrogen K-edge (400.0 eV) and the oxygen K-edge (531.7 eV) (*47*). Additional technical specifications are given in Kilcoyne et al. (*48*).

The MAXYMUS-STXM is located at the tunable undulator beamline UE46_PGM-2 at the BESSY II electron storage ring (1.7 GeV, multibunch mode) and provides a photon flux of ~$5 \cdot 10^8$ s^{-1} in the soft X-ray region. The undulator provides X-ray photons with selectable polarization in the range of 120-1900 eV. The STXM is equipped with a plane grating monochromator using a 600 l/mm blazed grating (resolving power $E/\Delta E \leq 8000$ at C-K), a Fresnel zone plate with 31 nm spatial resolution and a phosphor coated Lucite tube coupled with a photomultiplier. The samples were placed in an evacuated chamber (2-$5 \cdot 10^{-5}$ Pa). Further information can be found in Follath et al. (*49*).

Single energy images were recorded by raster-scanning the sample in the focused X-ray beam and measuring the intensity of transmitted monochromatic light as a function of sample position. X-ray absorption spectra were obtained either by recording a sequence of energy image scans or an energy line scan that sampled across the particle. For an energy image scan (“stack”) a series of images of a defined region with closely spaced photon energies is recorded over a certain energy range covering peak features, and with a coarser energy grid outside of the regions with fine structure. For line scans, the X-ray spot is scanned across a particle, then the photon energy is changed and the line rescanned. This yields a plot of transmitted light at each position on the scanned line as a function of energy. We used identical energy protocols (number of

energy points and spacings) for stacks and line scans, ranging from 270 to 600 eV, and spanning the carbon, potassium, calcium, nitrogen and oxygen edges (Fig. S2).

Based on the measured transmitted intensity *I(d)* the optical density *OD* was calculated applying Beer-Lambert's law (*50*):

$$OD = -\ln\left(\frac{I(d)}{I_0}\right) = \mu\rho d$$

where I_0 represents the incident photon flux, μ is the mass absorption coefficient, ρ is the sample density and d the sample thickness. I_0 was obtained as the transmission intensity through a particle free region of the substrate. For OD <1.5, particle sizes were in the linear absorption regime of the Beer-Lambert's law (*12*) which was assured for all particles reported in this study.

For the analysis of carbon NEXAFS spectra, the pre-edge absorption (mean value between 275 and 284 eV) was subtracted and the spectra were normalized by the carbon K-edge height (mean value between 305 and 320 eV) (*51*). We used fine structure features from resonant transitions of core electrons into excited states close to the ionization continuum (1s $\longrightarrow$ π^*, σ^*) to characterize the functional group composition of OA particles (50, *52*). Characteristic transitions are listed in Table S3.

For the analysis of atomic ratios (i.e., O:C, N:C) the heights of the C, N and O absorption edges ΔOD were determined as

$$\Delta OD = OD_{post-edge} - OD_{pre-edge}$$

with carbon post- and pre-edge energies being 320 and 280 eV; nitrogen: 425 and 395 eV; oxygen: 550 and 525 eV (*12*). The molar ratio of oxygen and carbon n_O/n_C is calculated as

$$\frac{n_O}{n_C} = \frac{\Delta OD_O M_C \mu_{C,post-pre}}{\Delta OD_C M_O \mu_{O,post-pre}}$$

with M as the atomic mass and $\mu_{post\text{-}pre}$ as the difference in mass absorption coefficient ($\mu_{C,320\text{-}280} = 3.8 \cdot 10^4$ cm^2 g^{-1}, $\mu_{N,425\text{-}395} = 2.8 \cdot 10^4$ cm^2 g^{-1}, $\mu_{O,550\text{-}525} = 2.0 \cdot 10^4$ cm^2 g^{-1}) (*12, 36-37, 47*). The ratio n_N/n_C is obtained in an analogous fashion. The calculation of n_O/n_C and n_N/n_C has been verified previously by Moffet et al. (*36*), and was reconfirmed in this study by means of organic standard compounds and aerosol mass spectrometry data for laboratory-generated SOA. The experimental results show good agreement with the theoretical ratios (see Table S4 and Sect. S2.2).

Based on non-normalized CNO spectra, the potassium mass fraction in organic particles was estimated as described in the following paragraph. In soft X-ray absorption spectra, the potassium $L_{3,2}$-absorption edge occurs as a characteristic double peak superimposed on the carbon K-edge absorption. Both closely spaced potassium L_3- and L_2-edges consist of pronounced and sharp peaks at the onset of the edge (at 297.4 eV and 299.9 eV) caused by the resonant electron transition from the ground states ($2p_{3/2}$, $2p_{1/2}$) into unoccupied states (3d) in addition to the actual absorption step function due to photo-ionization (*50*).

In spectra of OA particles with high potassium content, the pronounced potassium doublet and the height of the potassium absorption edge (relative to pre-edge absorption) are resolved. For OA particles with low potassium content only the potassium doublet is strong enough to be detected (Fig. S3). The height of the $L_{3,2}$-edge, ΔOD_{edge}, is proportional to the number of potassium atoms and can be used to quantify the potassium content. Based on 20 potassium-rich particles the following linear correlation ($R^2 = 0.85$) between ΔOD_{edge} and the height of the L_3-peak ΔOD_{L3} was established:

$$\Delta OD_{edge} = 0.235 \cdot \Delta OD_{L3}.$$

This correlation allowed a quantitative estimate of ΔOD_{edge} even for OA particles with low potassium content. The effective potassium detection limit in individual organic particles is given by the minimum ΔOD_{L3} that is resolvable above the spectral noise. It was estimated as ~2 fg. Based on Beer-Lambert's law, the following equation was used to calculate the absolute potassium mass, m_K, in individual aerosol particles:

$$m_K = \frac{\Delta OD_{edge} V}{0.7 \mu_{K,post-pre} h}$$

with V as the volume of the impacted OA droplets (= spherical cap), $\mu_{K,310\text{-}292} = 7.0 \cdot 10^4$ cm^2 g^{-1} as the difference in potassium L-edge mass absorption coefficient for the pre- and post-edge energies 292 and 310 eV (*47, 53*), h as the height of the impacted droplet, and a geometric factor of 0.7 to account for the average light path through the spherical cap (*12*). V can be calculated as

$$V = \frac{h\pi}{6}\left(3a^2 + h^2\right)$$

with a as the radius of the spherical cap that was measured for all particles based on STXM images (*54*). The height, h, is not directly accessible but can be estimated based on the measured

OD for C, N, and O. According to Pöschl et al. (*6*), C, N, and O account for ~80 % of the total mass, m_{total}, of Amazonian aerosol particles in the submicrometer size range. Therefore,

$$m_C + m_N + m_O = 0.8 m_{total}$$

with

$$m_X = \frac{OD_X V}{0.7 \mu_{X,post-pre} h}$$

and

$$m_{total} = V \cdot \rho$$

can be converted into

$$h = \frac{1}{0.56\rho}\left(\frac{OD_C}{\mu_C} + \frac{OD_N}{\mu_N} + \frac{OD_O}{\mu_O}\right).$$

Using ρ = 1.4 g cm^{-3} as a characteristic density value for OA particles (*2*), we obtained the radius-to-height ratio *a/h* with a mean value of ~10. Based on *a* and *a/h*, we calculated a volume equivalent diameter D_{ve} for each particle:

$$D_{ve} = \sqrt[3]{3ha^2 + h^3}\,.$$

According to Martin et al. (*5*), the fine organic aerosol mass concentration (<2 µm) during the wet season in the Amazon is of the order of ~2 µg m^{-3}. Multiplication of this value with an estimated average potassium mass fraction of ~2.6 % (median of all Amazonian OA particles analyzed in this study), yields an average atmospheric potassium concentration level of ~50 ng m^{-3} (estimated uncertainty: factor ~2), which is consistent with previous measurements (18-220 ng m^{-3}, (*16*)).

S1.6. SEM analysis

Scanning electron microscopy (SEM) images of aerosol particles were acquired using the secondary electron in-lens detector of a high-performance field emission instrument (LEO 1530 FESEM, EHT 10 keV, WD ~9 mm). The in-lens detector enabled detection of thin organic particles and coatings, which are often difficult to detect. The organic nature of SOA droplets and organic components of mixed SOA-inorganic particles were confirmed by NanoSIMS analysis as detailed below. Si_3N_4 windows are mounted on conductive Si wafers; however, the windows

themselves are nonconductive and show strong charging. Therefore, the back of the Si_3N_4 windows was coated with gold prior to SEM and NanoSIMS analysis to prevent charging and enhance the contrast of SOA particles against the substrate.

S1.7. NanoSIMS measurement and data processing

Chemical analysis of aerosol particles was performed using a Cameca NanoSIMS 50 ion microprobe in multi-collection detector mode by sputtering the sample with a ~1 pA Cs^+ primary ion beam focused into a spot of ~100 nm diameter. The primary ion beam was scanned several times over an area of 4 µm x 4 µm for the chemical analysis of standards, with a dwell time of 1000 µs $pixel^{-1}$, and images (256 x 256 pixels) were recorded for every scan. The detector dead time was 44 ns and the count rates were corrected accordingly. The energy bandpass slit was set to 20 eV, the entrance slit and aperture slit were decreased to 30 µm x 180 µm and 200 µm x 200 µm, respectively, and the transmission was kept at 50 % to enhance the count rate on small particles. A high transmission is possible because the influence of the quasi simultaneous arrival effect on the quantification of major elements is minor (<1 %) compared to the matrix effects, which introduce a ~20-40 % uncertainty.

On aerosol samples the field of vision was larger (10 µm x 10 µm) to view a representative area of the sample and compare with SEM and STXM images. To remove surface contaminations, all images were pre-sputtered for one cycle. The analysis time varied from 3-20 cycles depending on the number of scans required to collect an appropriate number of counts per pixel on each mass, and on the stability of the compounds investigated.

Secondary ions of $^{12}C^-$, $^{16}O^-$, $^{12}C_2^-$, $^{12}C^{14}N^-$, and $^{32}S^-$ were simultaneously collected in five electron multipliers on standards. For aerosol samples only one proxy for the carbon content of the sample ($^{12}C^-$ or $^{12}C_2^-$) was selected. Instead, $^{35}Cl^-$ was added to the list in order to allow the detection of a larger variety of inorganic salts. For quantification we compared normalized ion counts to the theoretical concentration of the species of interest in a large number of standards. The observed relationship was then used to calculate the concentration of the element of interest in the aerosol samples. This approach is straightforward for all samples that contain sufficient carbon atoms to ionize all of the nitrogen in the sample to CN^-. The logarithms of the observed calibration factors show a correlation ($R^2 = 0.99$) with the electron affinity that is similar to that

typically observed between the logarithm of the relative sensitivity factor (RSF) under Cs^+ bombardment and electron affinity (*55*).

For 19 salt-rich particles (<0.3 µm) from the aerosol samples ATTO_2011_#7 and ATTO_2011_#10 (Table S1) we determined approximate elemental mole fractions of carbon, nitrogen, oxygen, sulfur and chlorine (C:N:O:S:Cl = 0.01:0.09:0.62:0.17:0.02), indicating a relatively high abundance of sulfate ions in the salt core (Fig. S4, particles 1-3).

S1.8. WRF model simulation

In order to obtain the probability density distribution of vertical velocities, P_w, for the Amazonian region during the sampling period, the Weather Research & Forecast model (WRF-ARW-v3.3.1, http://www.mmm.ucar.edu/wrf/users/) was applied to simulate the meteorological conditions in the Amazon for the whole of May 2011. The model domain was horizontally configured as 299 × 249 grid cells with a spatial resolution of 9 km × 9 km. It was centered near Manaus, Brazil, and covers a large part of the Amazon forest region (Fig. S5). There were 34 vertical layers extending to 100 hPa (~15 km) with 17 layers below 4 km. To allow sufficient time for the model spin-up, we started the simulation on 26 April 2011. Meteorological initial and boundary conditions were interpolated from the NCEP-FNL Operational Global Analysis data (http://dss.ucar.edu/datasets/ds083.2/). The sea surface temperature was updated daily during the model simulation with real-time, global sea surface temperature analysis data (RTG_SST, ftp://polar.ncep.noaa.gov/pub/history/sst). MODIS land-use data with inland lake information were used to feed into the Noah Land Use scheme. Grid nudging was applied only for the spin-up period (April 26-30, 2011), and afterward the WRF model was set to run freely. An overview of the model configuration is given in Table S5.

S2 Supplementary Text

S2.1 Observations and sources of biogenic salt particles

The elemental composition of aerosol particles in the Amazon Basin during the wet season has been investigated previously, and a variety of different trace elements have been observed (*21, 25, 56-60*). In supermicrometer particles, two groups of elements have been found: (i) crustal elements such Si, Al, Ca, and Fe mostly from long range transport of Saharan dust, and (ii) "biogenic" elements such as S, K, and P (*25*). In submicrometer particles, the elements K, P, S, and Zn are frequently observed and mostly attributable to biogenic sources (*21-22, 60-61*). These elements often exhibit bimodal mass size distributions with relative maxima at ~0.3 µm and ~3 µm (*21, 25-26*). The night-time concentrations of K, P, and Zn usually exceed day-time concentrations due to increased microbiological activity (i.e., fungal spore release) during the night (*60*). Plants, fungi, and other microorganisms are considered to be potential sources of the potassium-salt-rich particles observed in this study (*16, 21, 25-26*). The following paragraph summarizes current knowledge about biogenic salt emission mechanisms from different organisms.

For the ejection of spores into the air, fungi have developed various active discharge mechanisms that involve hygroscopic water uptake by organic and inorganic solutes to generate osmotic pressure and surface tension effects. The active discharge of spores is accompanied by the emission of a liquid jet which contains inorganic ions and carbohydrates (*16*). Active wet discharge of *Ascomycota* spores utilizes osmotically pressurized small sacks (asci) which, upon bursting, eject spores and aqueous droplets of the osmotic fluid containing mannitol, potassium and chloride (*62*). Active wet discharge of *Basidiomycota* spores involves surface tension effects and aqueous droplets containing hexoses, mannitol, phosphate, sodium, and potassium (*63-64*). Elbert et al. (*16*) have shown that a major fraction of the potassium concentrations observed in the pristine Amazonian boundary layer can be explained by fungal emissions. X-ray and light microscopic analysis of our samples showed very high abundances of fungal spores in the coarse fraction, supporting the idea that fungal spore ejection is a plausible mechanism for the production of the observed potassium-rich particles (Fig. S6).

In addition to microorganism related emissions, the following plant related salt particle release mechanisms have been described in the literature: (I) transpiration, (II) guttation, (III) leaching of vegetation by rain, and (IV) particle release from leaves due to mechanical abrasion.

Beauford et al. (*29-30*) suggest that small biogenic salt particles can be released into the air by diffusiophoresis associated with water loss during rapid plant transpiration. Other studies provide experimental evidence that transpiration vapors from different plant species contain salt ions (e.g., Ca^{2+}, Na^{+}, K^{+}, NH_4^{+}; HCO_3^{-}, Cl^{-}, SO_4^{2-}) in considerable concentrations (up to 5 mg l^{-1} in the condensate) (*27, 65-67*).

Guttation is a common water release mechanism of plants when the water supply from the roots exceeds transpiration losses by the leaves. Since transpiration usually does not occur at night, leaf wetness frequently occurs in the morning hours, distinct from dew, depending on physiological and micrometeorological conditions (*68-69*). Guttation fluids (xylem sap) contain a mixture of sugars, amino acids, and salt ions, with particularly high K^{+}, Ca^{2+}, and Mg^{2+} content (15, *70*). Accordingly, guttation has been proposed as one potential origin of airborne trace elements in tropical environments (21, 28).

Leaching of soluble compounds from vegetation surfaces by rain, dew, and mist has been described in various studies (*71-73*). In addition to organic molecules (i.e., carbohydrates), the ions K^{+}, Ca^{2+}, Mg^{2+}, and Mn^{2+} are leached in the largest quantities (*73-74*). It has been suggested that leaching followed by droplet evaporation can generate airborne particles with high trace metal content (*66*).

Plant surfaces exposed to the atmosphere are covered with waxes that reduce the loss of water and act as a physical defense barrier against pathogens (*69*). In particular, epicuticular waxes often form the top layer of plant surfaces and are comprised of submicrometer sized, partly crystalline, particles (*75*). Such particles as small as 200 nm long and 30 nm wide can be released into the air when the plants are mechanically disturbed (e.g., due to rapid growth, surface abrasion by wind, or microbiological activity) (29-30, *76*).

The potassium-rich salt particles observed in this study (Fig. 1C-F) were typically in the size range of 0.1-0.3 µm. Figure S7 shows the size distribution obtained by SEM analysis of a morning sample with relatively high salt particle concentration. The maximum around 0.2 µm is in good agreement with the dilution trend of the potassium content in organic particles (Fig. 3). The grey shaded dilution band in Fig. 3 has been calculated assuming that primary biogenic salt particles in the size range of 0.1-0.3 µm with a density of 2.0-2.7 g cm^{-3} (KCl, K_2SO_4) (*77*) grew by condensation of SOA with a density of 1.0-1.4 g cm^{-3} (*2*). The calculated band covers almost

all data points and suggests that the size distribution shown in Fig. S7 is characteristic for the salt particles serving as seeds for the investigated Amazonian SOA.

S2.2 Validation of STXM elemental ratios

The stoichiometric ratios of organic standard compounds and the STXM elemental ratios for C, N, and O (n_O/n_C and n_N/n_C) generally show good agreement as previously verified by Moffet et al. (*36*). The results of this study confirm this observation and are summarized in Table S4. The STXM-NEXAFS and AMS derived elemental ratios for laboratory generated SOA show good agreement in n_O/n_C ratios with deviations up to 20 % (Table S4). For laboratory-generated SOA particles, ammonium sulfate [$(NH_4)_2SO_4$] seeds were added to the reaction chamber (Sect. S1.3). For isoprene SOA, ammonium sulfate accounts for a significant mass fraction of the resulting particles (7 % on average), and was observed in the form of a strong ammonium peak at the nitrogen absorption edge (Fig. S2). The mass fraction of ammonium sulfate for terpene SOA (3-4 %; Table S2) is much lower than that for isoprene SOA, corresponding to a weak ammonium peak at the nitrogen absorption edge (Fig. S2). For the STXM analysis, the amount of sulfate was quantified on the basis of the nitrogen content. Accordingly the n_O/n_C ratios were calculated for total oxygen (organics and sulfate) and for organic oxygen only. For the AMS analysis, the amount of sulfate is known and the n_O/n_C ratios were also derived for both cases, including and excluding sulfate.

S2.3 Internal structure, cloud/fog processing and CCN activation of aerosol particles

As discussed in the main text, the investigated Amazonian organic aerosol particles exhibited different types of internal structures that suggest a pronounced influence of cloud and fog processing on SOA formation and aging.

The organic bulk material of many OA_{mixed} particles shows a distinct core-shell structure with COOH-rich material in the core and C-OH-rich material in the shell (Fig. S4 and S8). This internal structure may be caused by cloud/fog processing, because OA_{acid} and $OA_{hydroxy}$, which are the main constituents of OA_{mixed}, have different solubilities in water. Upon evaporation of the cloud droplets, the less soluble OA_{acid} material would precipitate first, and the highly soluble hydroxy-rich material (probably sugar- or polyol-like) would form a viscous layer surrounding this core (*78*). In contrast, $OA_{hydroxy}$ occurs as chemically and morphologically homogenous

particles (Fig. S8C). Our findings are consistent with recent studies of liquid-liquid phase separation in organic and mixed organic-inorganic aerosol particles reporting a strong dependence on oxygen-to-carbon ratio of the organic material (*31-33*): Particles with low atomic ratios of oxygen-to-carbon tend to exhibit phase separation (O:C ≈ 0.5-0.7 in OA_{acid} and OA_{mixed}), which is not the case for particles with high O:C ratios (O:C ≈ 0.9-1.0 in $OA_{hydroxy}$; Table S4 and Fig. S8). The hygroscopic salt seeds as well as the variable chemical composition and morphology of the SOA particles suggest that aqueous phase reactions play an important role in particle growth and aging (*2, 79*).

To estimate the frequency of CCN activation and cloud droplet formation on Amazonian aerosol particles, we performed numerical model simulations using input parameters from this and related earlier studies (Sect. S1.8, (*6, 34*)). The ability of aerosol particles to act as CCN depends on the particle size, hygroscopicity, and water vapor supersaturation. To form cloud droplets, larger particles require a lower supersaturation, which corresponds to a lower updraft velocity (*6, 80-81*).

Figure S9 shows the critical updraft velocity for CCN activation of aerosol particles as a function of particle diameter. The curve results from cloud parcel model simulations with detailed spectral microphysics using parameters characteristic for pristine Amazonian aerosols during the wet season as determined in the AMAZE-08 campaign (pristine focus period) (*6, 39*): hygroscopicity parameter κ = 0.14; particle number concentration N = 200 cm^{-3}; number size distribution with two log-normal modes with a relative ratio of N_2/N_1 = 0.81 ($N = N_1 + N_2$) and with geometric mean diameter and standard deviation values of $D_{g,1}$ = 67 nm and $\sigma_{g,1}$ = 1.32 (Aitken mode) and $D_{g,2}$ = 150 nm and $\sigma_{g,2}$ = 1.43 (accumulation mode, see Fig. S10A).

As indicated by the dashed lines in Fig. S10A, updraft velocities >0.1 m s^{-1} are sufficient to activate accumulation mode particles at ~0.15 µm, whereas the CCN activation of Aitken mode particles at ~0.07 µm requires updraft velocities >1 m s^{-1}. Figure S11A shows the probability density function (P_w) of atmospheric vertical velocities (w) at different altitudes above the Amazonian rainforest during the wet season as calculated with the Weather Research and Forecast model (WRF-ARW-v3.3.1, Sect. S1.8) for the region and period around the aerosol sampling location and time (Fig. S5, May 2011). Combining P_w from Fig. S11A with w_{cri} from

Fig. S9, the probability of CCN activation for aerosol particles of a given size, $P_{act}(D_p)$, can be estimated as follows:

$$P_{act}(D_p) = \int_{w_{cri}}^{\infty} P_w \, dw \quad \text{with} \quad w_{cri} = f(D_p)$$

Figure S11B shows P_{act} for different altitudes plotted against the aerosol particle diameter. As expected, P_{act} is highest in the upper boundary layer (1-3 km) where the base of convective clouds usually forms. At altitudes ≥1 km, P_{act} is larger than ~0.5 % for diameters >0.1 µm, increases exponentially with increasing diameter, and exceeds 5 % for particles >0.15 µm, which account for most of the aerosol particle volume and mass (Fig. S10B) (*6*). In near-surface air (0.1-0.5 km), P_{act} is less than ~0.01 % for particles <0.1 µm, but it increases steeply and exceeds 0.5 % for particles >0.15 µm. The formation of low-lying cloud and fog over the rainforest is a common event in the wet season. The geometric mean value of P_{act} for the entire altitude range of 0.1-3 km can be regarded as an estimate for the effective average probability of CCN activation for aerosol particles in pristine Amazonian boundary layer air. It is multiple orders of magnitude higher for accumulation mode particles ($P_{act} \approx 2$ % for $D_p \approx 0.15$ µm) than for Aitken mode particles (P_{act} <0.01 % for $D_p \approx 0.07$ µm). This is consistent with the general assumption that the so-called Hoppel minimum around ~0.1 µm separating the Aitken mode and the accumulation mode in the size distribution of aged atmospheric aerosols is due to cloud processing (*82*).

In the size range >0.15 µm, which comprises the particles investigated in this study (Fig. 3) and represents the majority of SOA mass (*5*-*6*), the geometric mean value of P_{act} exceeds 2 %. The high probability of CCN activation underlines the importance of large accumulation mode particles for the formation of clouds over the rainforest, and it is consistent with the observation of core-shell structures indicating a pronounced influence of aqueous phase processing in clouds or fog on the formation and aging of SOA in the Amazon.

S2.4 Suppression of new particle formation in the Amazon

Numerous observations in the planetary boundary layer revealed a consistent correlation between sulfuric acid and the concentration of newly formed particles, and consequently sulfuric acid is thought to be the primary vapor responsible for atmospheric nucleation ((*83*-*86*) and references therein). Recent modeling studies argue convincingly that the concentration level of gaseous sulfuric acid in the Amazon region is too low to trigger nucleation and new particle

formation (NPF) events, in contrast to what is observed in relatively clean air over most other vegetated continental regions ((*8, 85, 87*) and references therein). In line with ambient observations, which consistently show that 10^6-10^7 molecules cm^{-3} of H_2SO_4 are necessary to produce particle formation events, laboratory studies reported that the threshold concentration of sulfuric acid at which newly formed particles (>3 nm) start to appear is approximately 5-$7 \cdot 10^6$ molecules cm^{-3} ((*85, 88*) and references therein). Kanawade et al. (*89*) calculated a H_2SO_4 concentration of about 1-$5 \cdot 10^5$ molecules cm^{-3} from the measured SO_2 (0.02-0.03 ppb) (*90*) and OH ($5.5 \cdot 10^6$ cm^{-3}) (*91*) over the Amazon basin, which is nearly one order of magnitude lower than the values observed in boreal forest in Finland (*92*) and in Michigan forest (*89*). Low- or semi-volatile organic vapors are also found to be involved in the nucleation and subsequent particle growth (*85*) and some laboratory studies reported that the presence of organics significantly enhances NPF (*93-95*). On the other hand, an experimental study showed that homo-molecular nucleation of organics, such as aromatic acids, in the absence of H_2SO_4 is unlikely to occur under atmospheric conditions (*93*). In addition, the relatively high isoprene-to-terpene ratio over the Amazon may play a role in suppressing nucleation as discussed by Kiendler-Scharr et al. (*96*) and Kanawade et al. (*89*). We assume that these and related issues of atmospheric gas phase chemistry are probably the main reason why NPF is not observed in the Amazon in contrast to boreal forest areas characterized by frequent NPF (*97-99*).

In addition, the presence of potassium-rich salt particles in a humid environment may indeed enhance the effective condensation sink of organic vapors as outlined below and may thus contribute to suppress new particle formation over the Amazon. The condensation sink (CS) of low-volatile vapors, as determined by the particle size distribution and surface concentration, in pristine Amazonian rainforest air is of the order of ~$1 \cdot 10^{-3}$ s^{-1} [based on the size distribution data of Zhou et al. (*100*) and Pöschl et al. (*6*)), the influence of hygroscopic growth at average RH of 93 % on the particles size distribution has been taken into account by using the measured average κ value during wet season of Amazon as 0.15 (*34*)]. Physically, the condensation sink in Amazonia is thus of similar magnitude as in pristine boreal forest air (CS = ~$4 \cdot 10^{-3}$ s^{-1} according to Kulmala et al. (*98*) and Kanawade et al. (*89*)). From a chemical perspective, however, aqueous droplets formed by hygroscopic growth of the potassium-rich salt particles in tropical rainforest air are not only a condensation sink for low-volatile vapors, they can also absorb volatile and semi-volatile organic compounds and provide a medium for multi-phase chemical reactions that

may be more efficient in converting VOC into SOA than gas phase chemical reactions followed by “dry condensation” of low-volatile vapors (*2*, *101-102*).

Thus, we suggest and intend to pursue further investigations to unravel and quantify how multi-phase chemistry on potassium-rich salt particles may influence the mechanism and rate of SOA formation and the apparent suppression of new particle formation (nucleation events) over the Amazon and other tropical rainforests compared to mid-latitude and boreal forests, which will require comprehensive field measurements of aerosol particle and precursor gas composition as well as kinetic process studies (laboratory experiments and model calculations).

References and Notes

1. J. L. Jimenez *et al*., Evolution of organic aerosols in the atmosphere. *Science* **326**, 1525 (2009). doi:10.1126/science.1180353 Medline

2. M. Hallquist *et al*., The formation, properties and impact of secondary organic aerosol: current and emerging issues. *Atmos. Chem. Phys.* **9**, 5155 (2009). doi:10.5194/acp-9-5155-2009

3. S. Solomon, *IPCC 4th Assessment Report* (Cambridge Univ. Press, Cambridge, 2007).

4. M. O. Andreae, Atmosphere. Aerosols before pollution. *Science* **315**, 50 (2007). doi:10.1126/science.1136529 Medline

5. S. T. Martin *et al*., Sources and properties of Amazonian aerosol particles. *Rev. Geophys.* **48**, RG2002 (2010). doi:10.1029/2008RG000280

6. U. Pöschl *et al*., Rainforest aerosols as biogenic nuclei of clouds and precipitation in the Amazon. *Science* **329**, 1513 (2010). doi:10.1126/science.1191056 Medline

7. Q. Chen *et al*., Mass spectral characterization of submicron biogenic organic particles in the Amazon Basin. *Geophys. Res. Lett.* **36**, L20806 (2009). doi:10.1029/2009GL039880

8. D. V. Spracklen *et al*., The contribution of boundary layer nucleation events to total particle concentrations on regional and global scales. *Atmos. Chem. Phys.* **6**, 5631 (2006). doi:10.5194/acp-6-5631-2006

9. R. Weigel *et al*., In situ observations of new particle formation in the tropical upper troposphere: the role of clouds and the nucleation mechanism. *Atmos. Chem. Phys.* **11**, 9983 (2011). doi:10.5194/acp-11-9983-2011

10. A. M. L. Ekman *et al*., Do organics contribute to small particle formation in the Amazonian upper troposphere? *Geophys. Res. Lett.* **35**, L17810 (2008). doi:10.1029/2008GL034970

11. Materials and methods are available as supplementary material on *Science* Online.

12. A. V. Tivanski, R. J. Hopkins, T. Tyliszczak, M. K. Gilles, Oxygenated interface on biomass burn tar balls determined by single particle scanning transmission X-ray microscopy. *J. Phys. Chem. A* **111**, 5448 (2007). doi:10.1021/jp070155u Medline

13. S. F. Maria, L. M. Russell, M. K. Gilles, S. C. B. Myneni, Organic aerosol growth mechanisms and their climate-forcing implications. *Science* **306**, 1921 (2004). doi:10.1126/science.1103491 Medline

14. M. Claeys *et al*., Formation of secondary organic aerosols through photooxidation of isoprene. *Science* **303**, 1173 (2004). doi:10.1126/science.1092805 Medline

15. J. L. Goatley, R. W. Lewis, Composition of guttation fluid from rye, wheat, and barley seedlings. *Plant Physiol.* **41**, 373 (1966). doi:10.1104/pp.41.3.373 Medline

16. W. Elbert, P. E. Taylor, M. O. Andreae, U. Pöschl, Contribution of fungi to primary biogenic aerosols in the atmosphere: Wet and dry discharged spores,

carbohydrates, and inorganic ions. *Atmos. Chem. Phys.* **7**, 4569 (2007). doi:10.5194/acp-7-4569-2007

17. M. O. Andreae, Soot carbon and excess fine potassium: long-range transport of combustion-derived aerosols. *Science* **220**, 1148 (1983). doi:10.1126/science.220.4602.1148 Medline

18. J. Li, M. Posfai, P. V. Hobbs, P. R. Buseck, Individual aerosol particles from biomass burning in southern Africa: 2, Compositions and aging of inorganic particles. *J. Geophys. Res.* **108**, 8484 (2003). doi:10.1029/2002JD002310

19. http://sigma.cptec.inpe.br/queimadas/v_anterior/dados_ant/dp_anteriores.html.

20. http://firefly.geog.umd.edu/firemap [Accessed 23 March 2012].

21. P. Artaxo, H. C. Hansson, Size distribution of biogenic aerosol particles from the Amazon Basin. *Atmos. Environ.* **29**, 393 (1995). doi:10.1016/1352-2310(94)00178-N

22. M. O. Andreae, P. J. Crutzen, Atmospheric aerosols: Biogeochemical sources and role in atmospheric chemistry. *Science* **276**, 1052 (1997). doi:10.1126/science.276.5315.1052

23. P. Artaxo, W. Maenhaut, H. Storms, R. Vangrieken, Aerosol characteristics and sources for the Amazon Basin during wet season. *J. Geophys. Res.* **95**, 16971 (1990). doi:10.1029/JD095iD10p16971

24. A. Worobiec *et al*., Characterisation of Amazon Basin aerosols at the individual particle level by X-ray microanalytical techniques. *Atmos. Environ.* **41**, 9217 (2007). doi:10.1016/j.atmosenv.2007.07.056

25. D. R. Lawson, J. W. Winchester, Sulfur, potassium, and phosphorus associations in aerosols from south-american tropical rain forests. *J. Geophys. Res.* **84**, 3723 (1979). doi:10.1029/JC084iC07p03723

26. D. R. Lawson, J. W. Winchester, Sulfur and trace-element concentration relationship in aerosols from south-american continent. *Geophys. Res. Lett.* **5**, 195 (1978). doi:10.1029/GL005i003p00195

27. G. E. Nemeryuk, Migration of salts into the atmosphere during transpiration. *Sov. Plant Physiol.* **17**, 560 (1970).

28. G. Crozat, Emission of potassium aerosols in tropical forest. *Tellus* **31**, 52 (1979). doi:10.1111/j.2153-3490.1979.tb00881.x

29. W. Beauford, J. Barber, A. R. Barringer, Release of particles containing metals from vegetation into the atmosphere. *Science* **195**, 571 (1977). doi:10.1126/science.195.4278.571 Medline

30. W. Beauford, J. Barber, A. R. Barringer, Heavy metal release from plants into the atmosphere. *Nature* **256**, 35 (1975). doi:10.1038/256035a0 Medline

31. A. K. Bertram *et al*., Predicting the relative humidities of liquid-liquid phase separation, efflorescence, and deliquescence of mixed particles of ammonium sulfate, organic material, and water using the organic-to-sulfate mass ratio of the

particle and the oxygen-to-carbon elemental ratio of the organic component. *Atmos. Chem. Phys.* **11**, 10995 (2011). doi:10.5194/acp-11-10995-2011

32. M. Song, C. Marcolli, U. K. Krieger, A. Zuend, T. Peter, Liquid-liquid phase separation and morphology of internally mixed dicarboxylic acids/ammonium sulfate/water particles. *Atmos. Chem. Phys.* **12**, 2691 (2012). doi:10.5194/acp-12-2691-2012

33. A. Zuend, J. H. Seinfeld, Modeling the gas-particle partitioning of secondary organic aerosol: The importance of liquid-liquid phase separation. *Atmos. Chem. Phys.* **12**, 3857 (2012). doi:10.5194/acp-12-3857-2012

34. S. S. Gunthe *et al*., Cloud condensation nuclei in pristine tropical rainforest air of Amazonia: Size-resolved measurements and modeling of atmospheric aerosol composition and CCN activity. *Atmos. Chem. Phys.* **9**, 7551 (2009). doi:10.5194/acp-9-7551-2009

35. L. M. Russell, S. F. Maria, S. C. B. Myneni, Mapping organic coatings on atmospheric particles. *Geophys. Res. Lett.* **29**, 1779 (2002). doi:10.1029/2002GL014874

36. R. C. Moffet, A. V. Tivanski, M. K. Gilles, in *Fundamentals and Applications in Aerosol Apectroscopy*, R. Signorell, J. Reid, Eds. (CRC, Boca Raton, FL, 2010).

37. R. J. Hopkins, A. V. Tivanski, B. D. Marten, M. K. Gilles, Chemical bonding and structure of black carbon reference materials and individual carbonaceous atmospheric aerosols. *J. Aerosol Sci.* **38**, 573 (2007). doi:10.1016/j.jaerosci.2007.03.009

38. D. Solomon *et al*., Carbon (1s) NEXAFS Spectroscopy of biogeochemically relevant reference organic compounds. *Soil Sci. Soc. Am. J.* **73**, 1817 (2009). doi:10.2136/sssaj2008.0228

39. S. T. Martin *et al*., An overview of the Amazonian aerosol characterization experiment 2008 (AMAZE-08). *Atmos. Chem. Phys.* **10**, 11415 (2010). doi:10.5194/acp-10-11415-2010

40. S. M. King, T. Rosenoern, J. E. Shilling, Q. Chen, S. T. Martin, Increased cloud activation potential of secondary organic aerosol for atmospheric mass loadings. *Atmos. Chem. Phys.* **9**, 2959 (2009). doi:10.5194/acp-9-2959-2009

41. P. F. DeCarlo *et al*., Field-deployable, high-resolution, time-of-flight aerosol mass spectrometer. *Anal. Chem.* **78**, 8281 (2006). doi:10.1021/ac061249n Medline

42. Q. Chen, Y. Liu, N. M. Donahue, J. E. Shilling, S. T. Martin, Particle-phase chemistry of secondary organic material: modeled compared to measured O:C and H:C elemental ratios provide constraints. *Environ. Sci. Technol.* **45**, 4763 (2011). doi:10.1021/es104398s Medline

43. J. E. Shilling *et al*., Particle mass yield in secondary organic aerosol formed by the dark ozonolysis of alpha-pinene. *Atmos. Chem. Phys.* **8**, 2073 (2008). doi:10.5194/acp-8-2073-2008

44. Q. Chen, Y. L. Li, K. A. McKinney, M. Kuwata, S. T. Martin, Particle mass yield from β-caryophyllene ozonolysis. *Atmos. Chem. Phys.* **12**, 3165 (2012). doi:10.5194/acp-12-3165-2012

45. S. M. King *et al*., Cloud droplet activation of mixed organic-sulfate particles produced by the photooxidation of isoprene. *Atmos. Chem. Phys.* **10**, 3953 (2010). doi:10.5194/acp-10-3953-2010

46. M. Fierz, R. Kaegi, H. Burtscher, Theoretical and experimental evaluation of a portable electrostatic TEM sampler. *Aerosol Sci. Technol.* **41**, 520 (2007). doi:10.1080/02786820701253327

47. B. L. Henke, P. Lee, T. J. Tanaka, R. L. Shimabukuro, B. K. Fujikawa, Low-energy X-ray interaction coefficients: photoabsorption, scattering, and reflection. *At. Data Nucl. Data Tables* **27**, 1 (1982). doi:10.1016/0092-640X(82)90002-X

48. A. L. D. Kilcoyne *et al*., Interferometer-controlled scanning transmission X-ray microscopes at the Advanced Light Source. *J. Synchrotron Radiat.* **10**, 125 (2003). doi:10.1107/S0909049502017739 Medline

49. R. Follath, J. S. Schmidt, M. Weigand, K. Fauth, in *Sri 2009: The 10th International Conference on Synchrotron Radiation Instrumentation*, R. Garrett, I. Gentle, K. Nugent, S. Wilkins, Eds. (American Institute of Physics, Melville, NY, 2010), vol. 1234, pp. 323–326.

50. J. Stöhr, *NEXAFS Spectroscopy* (Springer-Verlag, Berlin, ed. 1, 2003).

51. S. Takahama, S. Liu, L. M. Russell, Coatings and clusters of carboxylic acids in carbon-containing atmospheric particles from spectromicroscopy and their implications for cloud-nucleating and optical properties. *J. Geophys. Res.* **115**, D01202 (2010). doi:10.1029/2009JD012622

52. S. C. B. Myneni, in *Applications of Synchrotron Radiation in Low-Temperature Geochemistry and Environmental Sciences*, P. A. Fenter, M. L. Rivers, N. C. Sturchio, S. R. Sutton, Eds. (Mineralogical Society of America, Washington, DC, 2002), vol. 49, pp. 485–579.

53. B. L. Henke, E. M. Gullikson, J. C. Davis, X-ray interactions - photoabsorption, scattering, transmission, and refelction at E=50-30,000 eV, Z=1-92. *At. Data Nucl. Data Tables* **54**, 181 (1993). doi:10.1006/adnd.1993.1013

54. L. Råde, B. Westergren, *Mathematics Handbook for Science and Engineering* (Springer, Berlin, ed. 5, 2004).

55. A. Benninghoven, F. G. Rüdenauer, H. W. Werner, *Secondary Ion Mass Spectrometry: Basic Concepts, Instrumental Aspects, Applications, and Trends* (Wiley, New York, 1987).

56. W. Maenhaut, M. T. Fernandez-Jimenez, I. Rajta, P. Artaxo, Two-year study of atmospheric aerosols in Alta Floresta, Brazil: Multielemental composition and source apportionment. *Nucl. Instrum. Methods Phys. Res. B* **189**, 243 (2002). doi:10.1016/S0168-583X(01)01050-3

57. F. Echalar *et al*., Long-term monitoring of atmospheric aerosols in the Amazon Basin: Source identification and apportionment. *J. Geophys. Res.* **103**, 31849 (1998). doi:10.1029/98JD01749

58. L. Wouters, S. Hagedoren, I. Dierck, P. Artaxo, R. Vangrieken, Laser microprobe mass analysis of Amazon Basin aerosols. *Atmos. Environ.* **27**, 661 (1993). doi:10.1016/0960-1686(93)90184-Z

59. P. Artaxo *et al*., Physical and chemical properties of aerosols in the wet and dry seasons in Rondonia, Amazonia. *J. Geophys. Res.* **107**, 8081 (2002). doi:10.1029/2001JD000666

60. B. Graham *et al*., Composition and diurnal variability of the natural Amazonian aerosol. *J. Geophys. Res.* **108**, 4765 (2003). doi:10.1029/2003JD004049

61. S. Matthias-Maser, R. Jaenicke, The size distribution of primary biological aerosol particles with radii >0.2 μm in an urban rural influenced region. *Atmos. Res.* **39**, 279 (1995). doi:10.1016/0169-8095(95)00017-8

62. F. Trail, I. Gaffoor, S. Vogel, Ejection mechanics and trajectory of the ascospores of *Gibberella zeae* (anamorph *Fuarium graminearum*). *Fungal Genet. Biol.* **42**, 528 (2005). doi:10.1016/j.fgb.2005.03.008 Medline

63. J. C. R. Turner, J. Webster, Mushroom Spores - The analysis of Bullers drop. *Chem. Eng. Sci.* **50**, 2359 (1995). doi:10.1016/0009-2509(95)00097-O

64. J. Webster *et al*., Mannitol and hexoses are components of Bullers drop. *Mycol. Res.* **99**, 833 (1995). doi:10.1016/S0953-7562(09)80737-5

65. A. A. Kazarov, L. S. Plieva, Evolution of ions into the atmosphere during transpiration by plants of several zones of the Northern Caucasus. *Sov. Plant Physiol.* **36**, 761 (1989).

66. G. C. Curtin, H. D. King, E. L. Mosier, Movement of elements into the atmosphere from coniferous trees in subalpine forests of colorado and Idaho. *J. Geochem. Explor.* **3**, 245 (1974). doi:10.1016/0375-6742(74)90025-9

67. Y. L. Melchakov, Ecological and geochemical effect of evapotranspiration in the mountain-taiga and subalpine belts of the Northern Urals. *Geochem. Int.* **50**, 84 (2012). doi:10.1134/S0016702911110073

68. R. N. Hughes, P. Brimblecombe, Dew and guttation - Formation and environmental significance. *Agric. For. Meteorol.* **67**, 173 (1994). doi:10.1016/0168-1923(94)90002-7

69. L. Taiz, E. Zeiger, *Plant Physiology* (Sinauer, Sunderland, MA, 2010).

70. N. Mizuno, A. Takahashi, T. Wagatsuma, T. Mizuno, H. Obata, Chemical composition of guttation fluid and leaves of Petasites japonicus v. giganteus and Polygonum cuspidatum growing on ultramafic soil. *Soil Sci. Plant Nutr.* **48**, 451 (2002). doi:10.1080/00380768.2002.10409225

71. G. M. Will, Removal of mineral nutrients from tree crowns by rain. *Nature* **176**, 1180 (1955). doi:10.1038/1761180b0

72. H. B. Tukey, R. A. Mecklenburg, Leaching of metabolites from foliage + subsequent reabsorption + redistribution of leachate in plants. *Am. J. Bot.* **51**, 737 (1964). doi:10.2307/2440213

73. H. B. Tukey, Jr., Leaching of substances from plants. *Annu. Rev. Plant Physiol.* **21**, 305 (1970). doi:10.1146/annurev.pp.21.060170.001513

74. G. Stenlid, Salt losses and redistribution of salts in higher plants, in *Encyclopedia of Plant Physiology*, W. Ruhland, Ed. (Springer, Berling, 1958), vol. 4, pp. 615–637.

75. S. D. Eigenbrode, K. A. Stoner, A. M. Shelton, W. C. Kain, Characteristics of glossy leaf waxes associated with resistance to diamondback moth (lepidoptera, plutellidae) in brassica-oleracea. *J. Econ. Entomol.* **84**, 1609 (1991).

76. J. T. Martin, B. E. Juniper, *The Cuticles of Plants* (Publisher, City, 1970).

77. D. R. Lide, *CRC Handbook of Chemistry and Physics* (CRC, Boca Raton, FL, ed. 92, 2011).

78. M. Shiraiwa, M. Ammann, T. Koop, U. Pöschl, Gas uptake and chemical aging of semisolid organic aerosol particles. *Proc. Natl. Acad. Sci. U.S.A.* **108**, 11003 (2011). doi:10.1073/pnas.1103045108 Medline

79. Y. B. Lim, Y. Tan, M. J. Perri, S. P. Seitzinger, B. J. Turpin, Aqueous chemistry and its role in secondary organic aerosol (SOA) formation. *Atmos. Chem. Phys.* **10**, 10521 (2010). doi:10.5194/acp-10-10521-2010

80. M. O. Andreae, D. Rosenfeld, Aerosol-cloud-precipitation interactions. Part 1. The nature and sources of cloud-active aerosols. *Earth Sci. Rev.* **89**, 13 (2008). doi:10.1016/j.earscirev.2008.03.001

81. P. Reutter *et al*., Aerosol- and updraft-limited regimes of cloud droplet formation: influence of particle number, size and hygroscopicity on the activation of cloud condensation nuclei (CCN). *Atmos. Chem. Phys.* **9**, 7067 (2009). doi:10.5194/acp-9-7067-2009

82. J. H. Seinfeld, S. N. Pandis, *Atmospheric Chemistry and Physics* (Wiley, New York, 1998).

83. M. Sipilä *et al*., The role of sulfuric acid in atmospheric nucleation. *Science* **327**, 1243 (2010). doi:10.1126/science.1180315 Medline

84. J. Kirkby *et al*., Role of sulphuric acid, ammonia and galactic cosmic rays in atmospheric aerosol nucleation. *Nature* **476**, 429 (2011). doi:10.1038/nature10343 Medline

85. A. Metzger *et al*., Evidence for the role of organics in aerosol particle formation under atmospheric conditions. *Proc. Natl. Acad. Sci. U.S.A.* **107**, 6646 (2010). doi:10.1073/pnas.0911330107 Medline

86. M. Kulmala, Atmospheric science. How particles nucleate and grow. *Science* **302**, 1000 (2003). doi:10.1126/science.1090848 Medline

87. F. Yu, G. Luo, Simulation of particle size distribution with a global aerosol model: contribution of nucleation to aerosol and CCN number concentrations. *Atmos. Chem. Phys.* **9**, 7691 (2009). doi:10.5194/acp-9-7691-2009

88. T. Berndt, O. Böge, F. Stratmann, J. Heintzenberg, M. Kulmala, Rapid formation of sulfuric acid particles at near-atmospheric conditions. *Science* **307**, 698 (2005). doi:10.1126/science.1104054 Medline

89. V. P. Kanawade *et al*., Isoprene suppression of new particle formation in a mixed deciduous forest. *Atmos. Chem. Phys.* **11**, 6013 (2011). doi:10.5194/acp-11-6013-2011

90. M. O. Andreae, T. W. Andreae, The cycle of biogenic sulfur-compounds over the Amazon Basin. 1. Dry season. *J. Geophys. Res.* **93**, 1487 (1988). doi:10.1029/JD093iD02p01487

91. M. Martinez *et al*., Hydroxyl radicals in the tropical troposphere over the Suriname rainforest: Airborne measurements. *Atmos. Chem. Phys.* **10**, 3759 (2010). doi:10.5194/acp-10-3759-2010

92. T. Petäjä *et al*., Sulfuric acid and OH concentrations in a boreal forest site. *Atmos. Chem. Phys.* **9**, 7435 (2009). doi:10.5194/acp-9-7435-2009

93. R. Y. Zhang *et al*., Atmospheric new particle formation enhanced by organic acids. *Science* **304**, 1487 (2004). doi:10.1126/science.1095139 Medline

94. R. Zhang *et al*., Formation of nanoparticles of blue haze enhanced by anthropogenic pollution. *Proc. Natl. Acad. Sci. U.S.A.* **106**, 17650 (2009). doi:10.1073/pnas.0910125106 Medline

95. B. Verheggen *et al*., Alpha-pinene oxidation in the presence of seed aerosol: estimates of nucleation rates, growth rates, and yield. *Environ. Sci. Technol.* **41**, 6046 (2007). doi:10.1021/es070245c Medline

96. A. Kiendler-Scharr *et al*., New particle formation in forests inhibited by isoprene emissions. *Nature* **461**, 381 (2009). doi:10.1038/nature08292 Medline

97. M. Dal Maso *et al*., Formation and growth of fresh atmospheric aerosols: Eight years of aerosol size distribution data from SMEAR II, Hyytiala, Finland. *Boreal Env. Res.* **10**, 323 (2005).

98. M. Kulmala *et al*., On the formation, growth and composition of nucleation mode particles. *Tellus* **53**, 479 (2001). doi:10.1034/j.1600-0889.2001.d01-33.x

99. M. Kulmala *et al*., Formation and growth rates of ultrafine atmospheric particles: A review of observations. *J. Aerosol Sci.* **35**, 143 (2004). doi:10.1016/j.jaerosci.2003.10.003

100. J. Zhou, E. Swietlicki, H. C. Hansson, P. Artaxo, Submicrometer aerosol particle size distribution and hygroscopic growth measured in the Amazon rain forest during the wet season. *J. Geophys. Res.* **107**, 8055 (2002). doi:10.1029/2000JD000203

101. A. G. Carlton, C. Wiedinmyer, J. H. Kroll, A review of secondary organic aerosol (SOA) formation from isoprene. *Atmos. Chem. Phys.* **9**, 4987 (2009). doi:10.5194/acp-9-4987-2009

102. B. Ervens, B. J. Turpin, R. J. Weber, Secondary organic aerosol formation in cloud droplets and aqueous particles (aqSOA): A review of laboratory, field and model studies. *Atmos. Chem. Phys.* **11**, 11069 (2011). doi:10.5194/acp-11-11069-2011

103. T. H. Yoon *et al*., Nanometer-scale chemical heterogeneities of black carbon materials and their impacts on PCB sorption properties: soft X-ray spectromicroscopy study. *Environ. Sci. Technol.* **40**, 5923 (2006). doi:10.1021/es060173+ Medline

104. S. Takahama, S. Gilardoni, L. M. Russell, A. L. D. Kilcoyne, Classification of multiple types of organic carbon composition in atmospheric particles by scanning transmission X-ray microscopy analysis. *Atmos. Environ.* **41**, 9435 (2007). doi:10.1016/j.atmosenv.2007.08.051

105. A. P. Serro, A. C. Fernandes, B. Saramago, J. Lima, M. A. Barbosa, Apatite deposition on titanium surfaces—the role of albumin adsorption. *Biomaterials* **18**, 963 (1997). doi:10.1016/S0142-9612(97)00031-8 Medline

106. W. C. Skamarock *et al*., "A description of the advanced research WRF version 3" [National Center for Atmospheric Research (NCAR) Technical Note, NCAR/TN-475-STR, Boulder, CO, 2008].

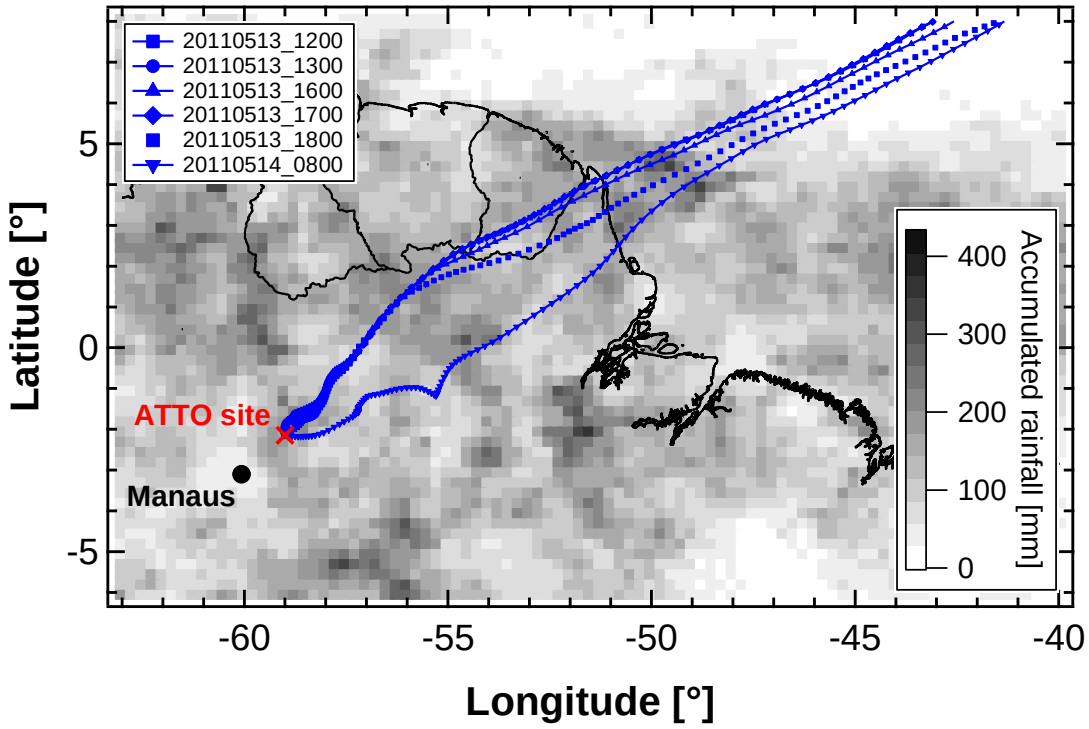

Figure S1. Location of the ATTO site in central Amazonia, Brazil, with back trajectories (HYSPLIT, NOAA-ARL, GDAS1 model, start height 100 m) and cumulative rainfall (tropical rainfall measuring mission TRMM) from 13 to 17 May 2011. Back trajectories are simulated for sampling time of individual impactor samples (Table S1).

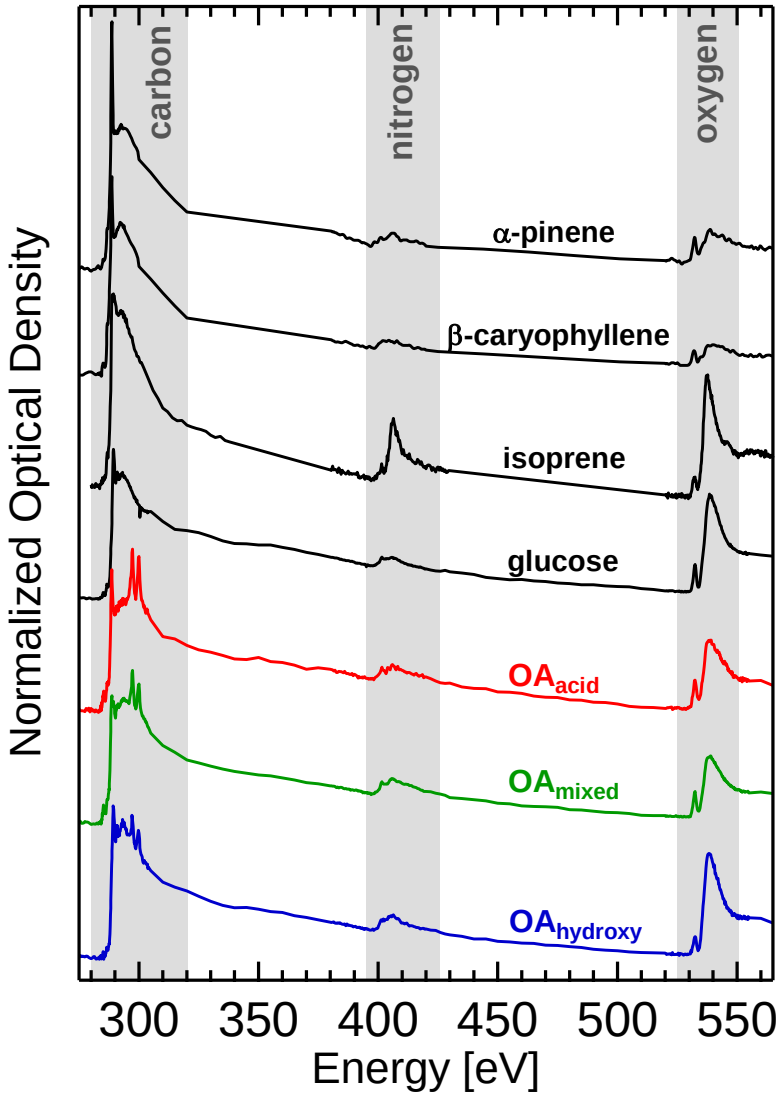

Figure S2. CNO X-ray absorption spectra of (i) laboratory-generated SOA from terpene (*α*-pinene and *β*-caryophyllene) and isoprene oxidation, (ii) glucose as reference compound from spray-drying of aqueous solution and (iii) Amazonian OA particles (OA_{acid}, OA_{mixed}, $OA_{hydroxy}$). The spectra cover the K-edges of carbon (283.8 eV), nitrogen (400.0 eV) and oxygen (531.7 eV) as well as the $L_{3,2}$-edges of potassium (294.6 eV) and calcium (349.3 eV). The carbon edge fine structure for the same spectra is shown in Fig. 2A.

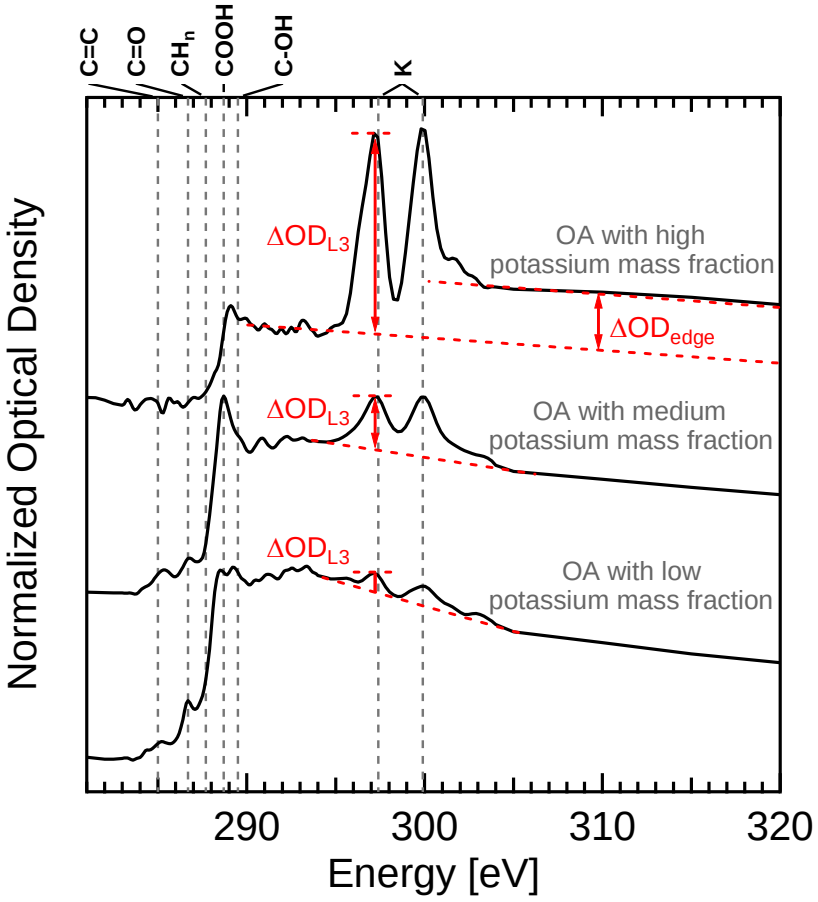

Figure S3. Characteristic spectra of individual Amazonian aerosol particles with different potassium mass fractions. Parameters ΔOD_{edge} and ΔOD_{L3} are used for potassium quantification.

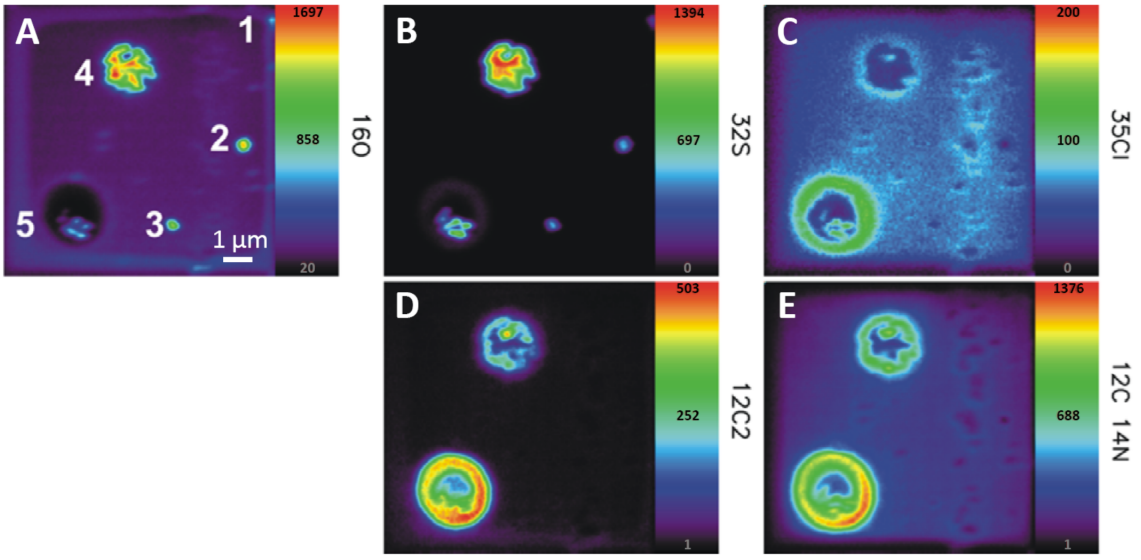

Figure S4. NanoSIMS images exhibiting elemental maps for (**A**) oxygen, (**B**) sulfur, (**C**) chlorine, (**D**) carbon, and (**E**) nitrogen of Amazonian aerosol particles. 1, 2, and 3 are small salt-rich particles. 4 and 5 are large OA particles exhibiting pronounced core-shell structures. Color code indicates counts of secondary ions.

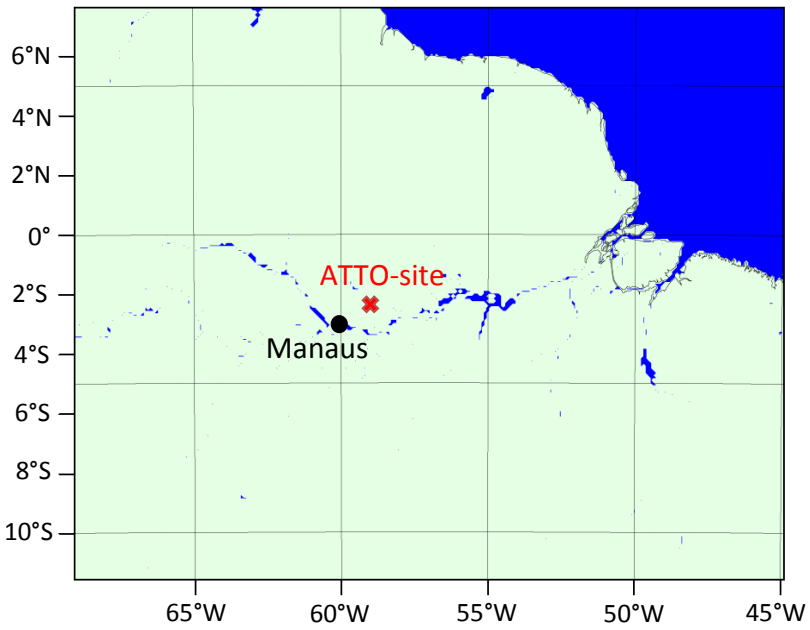

Figure S5. WRF model domain around the sampling location (ATTO site). Updraft velocities were calculated for May 2011 and integrated over the entire rainforest area (green shading).

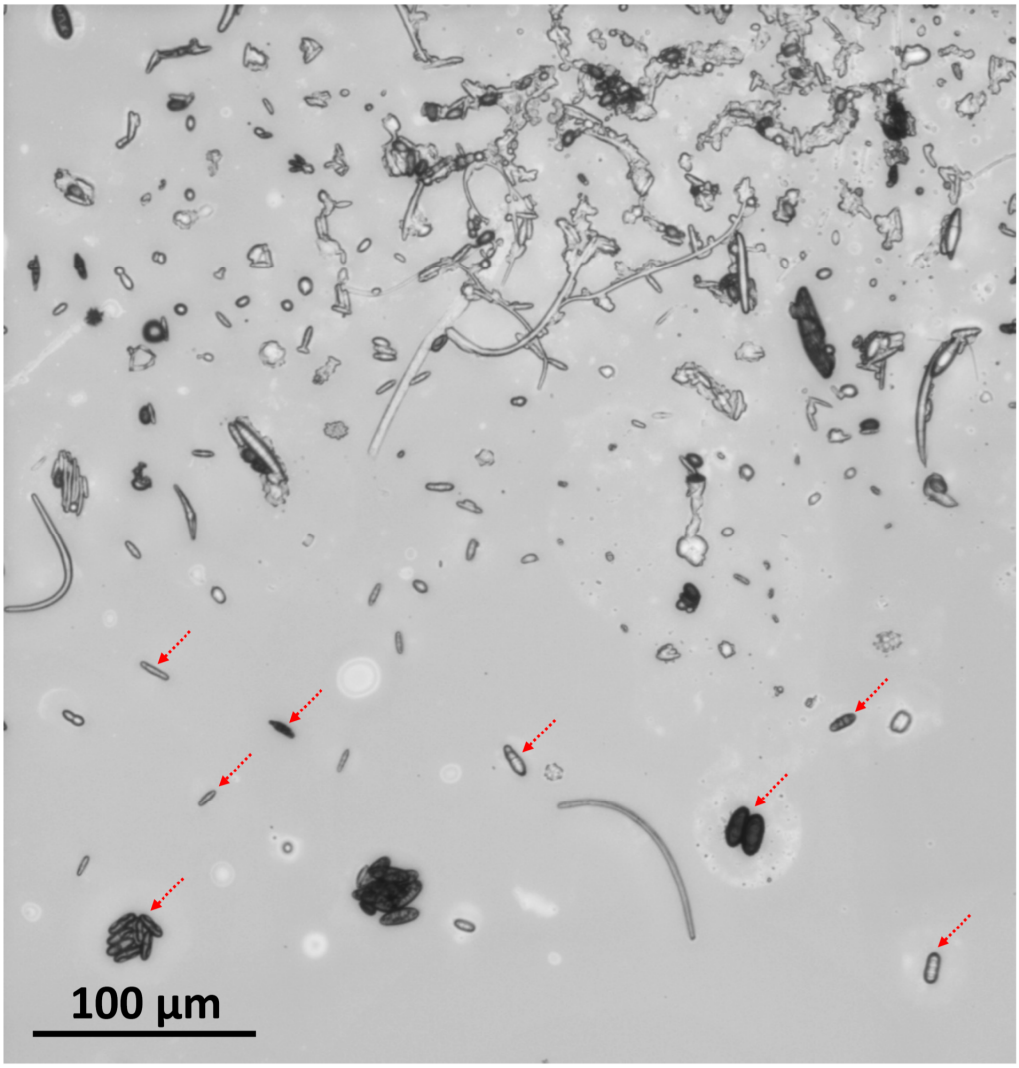

Figure S6. Light microscopy image of coarse mode particles in Amazonian aerosol sample (ATTO_2011_#2; Table S1). A high abundance and diversity of fungal spores was observed (examples are indicated by red arrows).

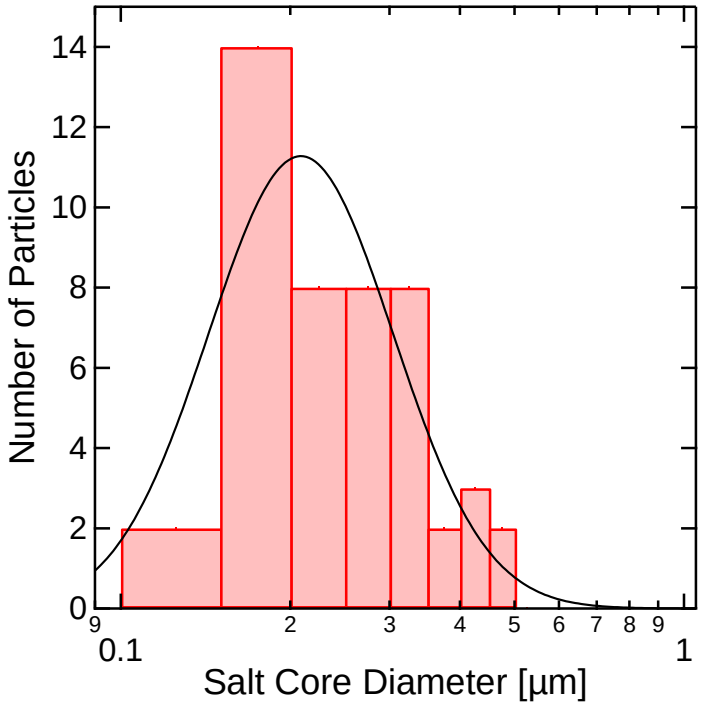

Figure S7. Size distribution of salt cores in the Amazonian aerosol sample ATTO_2011_#10 collected in the morning of 14 May 2011 (Table S1, Sect. 2.1). SEM measurement data (red bars) and lognormal fit (black line) indicate a peak around ~0.2 µm.

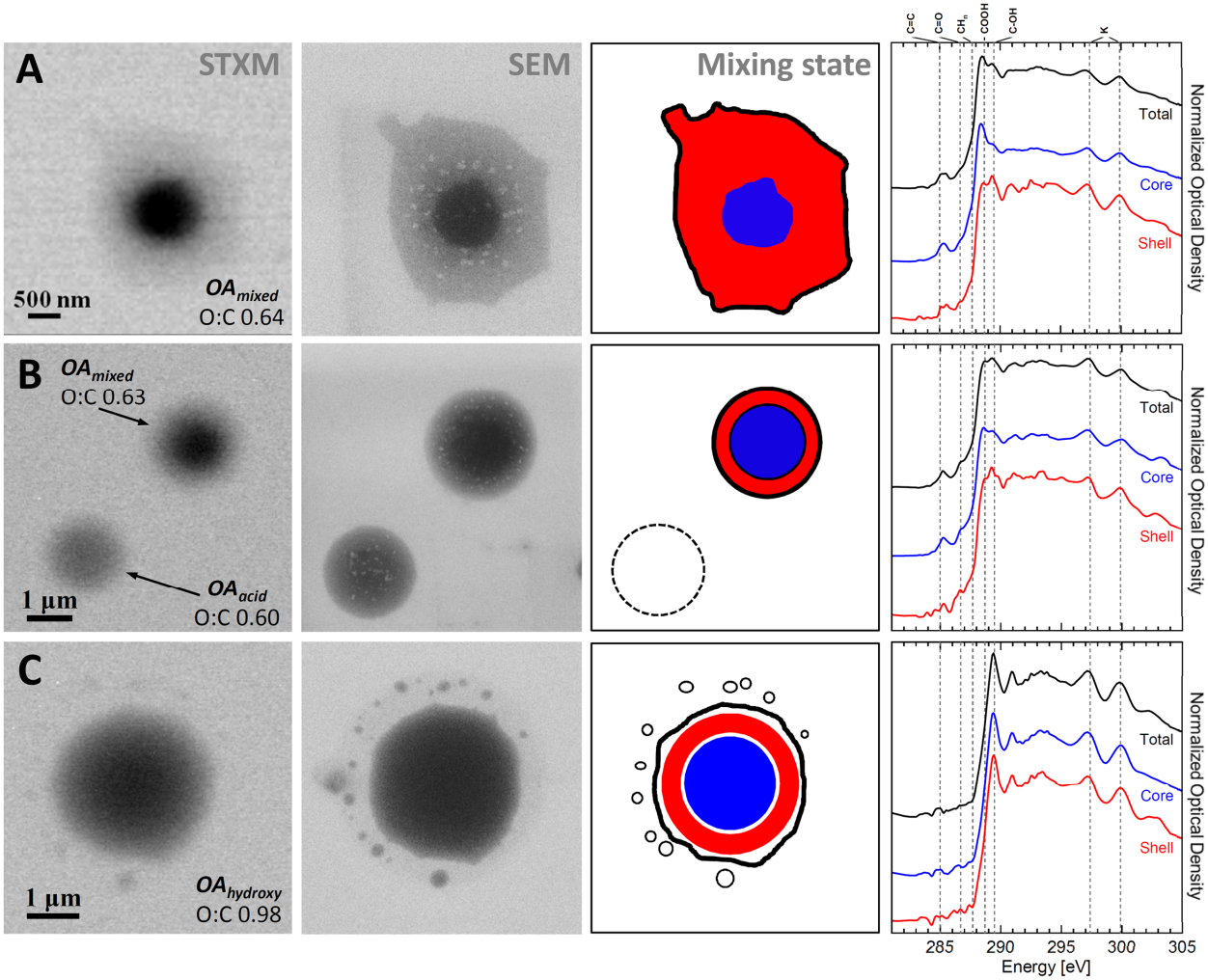

Figure S8. Internal structures of Amazonian organic aerosol particles analyzed by STXM-NEXAFS and SEM. Color code indicates integrated region for corresponding NEXAFS spectra. (**A**) OA_{mixed} particle with COOH-rich core and thick C-OH-rich coating. (**B**) OA_{mixed} particle with COOH-rich core and thin C-OH-rich coating. (**C**) $OA_{hydroxy}$ with homogenous chemical composition. Halos of small satellite droplets were observed for ~50 % of $OA_{hydroxy}$ particles (O:C ≈ 0.9-1.0) but not for OA_{acid} and OA_{mixed} particles (O:C ≈ 0.5-0.7). The halo satellite droplets were not considered in quantitative analyses of particle size distribution and potassium content.

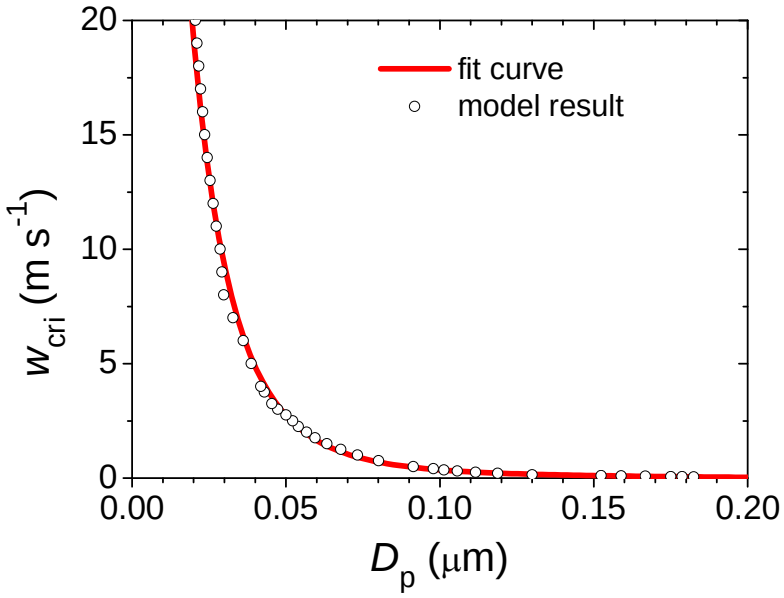

Figure S9. Critical updraft velocity for CCN activation of aerosol particles as a function of particle diameter. The data points are the results of cloud parcel model simulations with detailed spectral microphysics using parameters characteristic for pristine Amazonian aerosols (*6, 34*). The line is a fit of the form $w_{cri} = f(D_p)$ =10^(-452·D_p^3+208·D_p^2 -40.93·D_p+2.021).

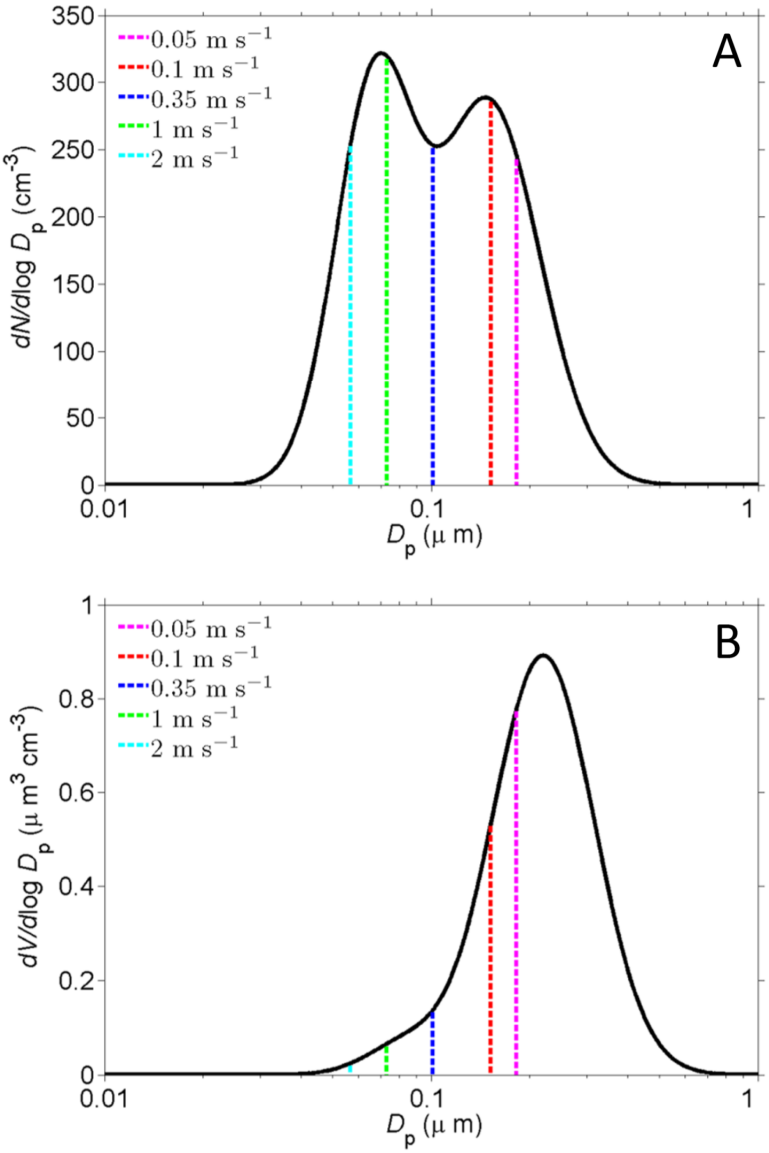

Figure S10. Aerosol size distribution and critical diameters of CCN activation for different updraft velocities (w = 0.05 to 2 m s^{-1}) characteristic for pristine Amazonian aerosols. (**A**) Particle number distribution composed of an Aitken mode around ~0.07 µm and an accumulation mode around ~0.15 µm (*6*, *34*). (**B**) Particle volume distribution corresponding to the bimodal number distribution shown in panel A. Note that the actual volume distribution around 1 µm is higher because of coarse particles (primary biological material and mineral dust (*6*)) that are not included in this analysis, which is focused on the SOA particles dominating the accumulation mode composition.

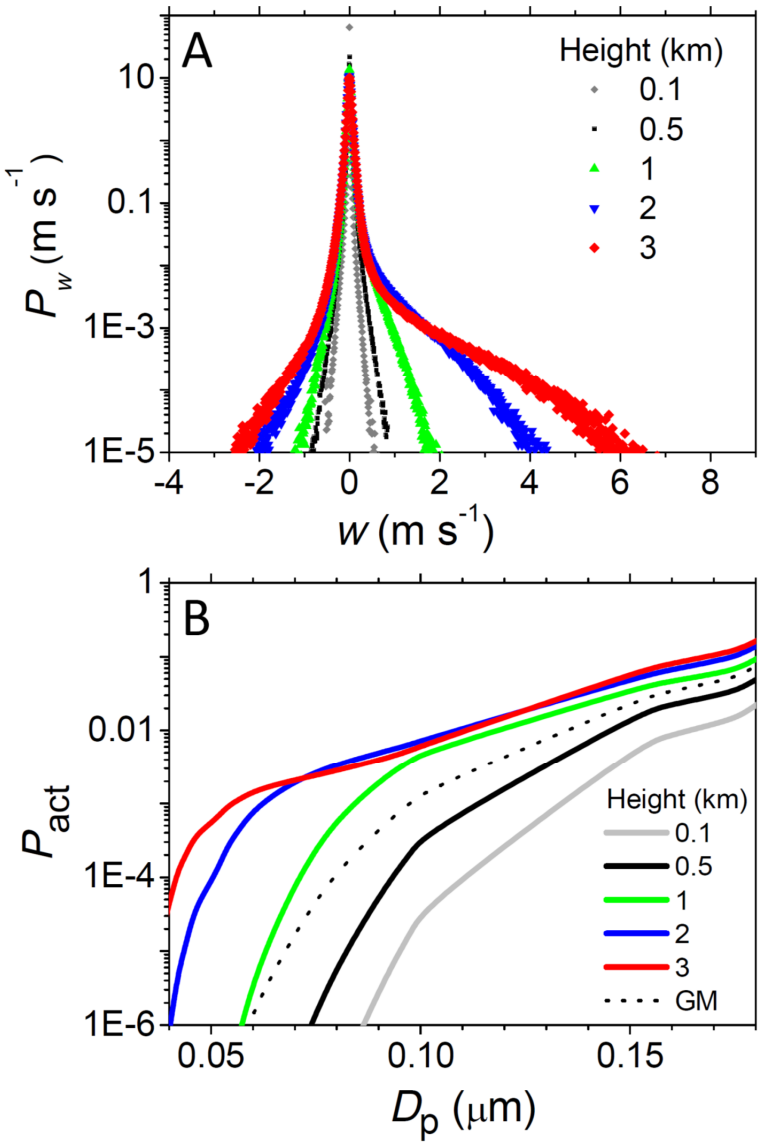

Figure S11. (**A**) Probability density function, P_w, of atmospheric updraft velocity, w, at different altitudes above the Amazonian rainforest during the wet season as calculated with the Weather Research and Forecast model (WRF-ARW-v3.3.1, Sect. S1.8) for the region and period around the aerosol sampling location and time (Fig. S5, May 2011). (**B**) CCN activation probability, P_{act}, of particles at diameter D_p. The lines represent results at different heights (GM = geometric mean value).

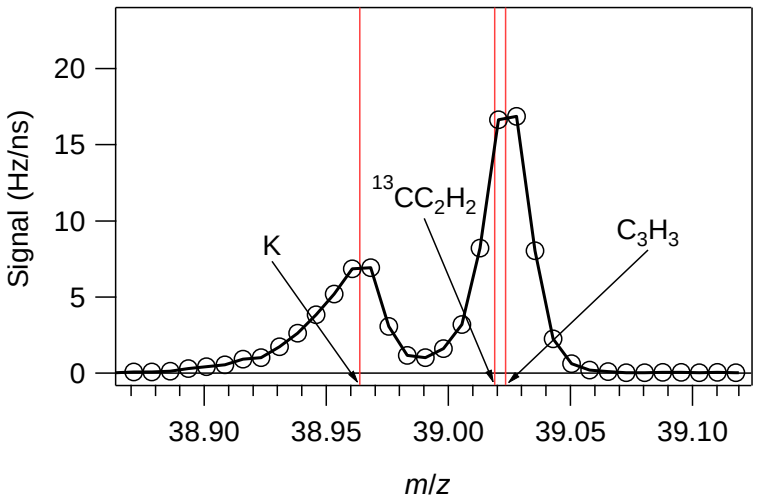

Figure S12. Particle mass spectrum averaged for pristine conditions during AMAZE-08 ("class I"), as detected by high-resolution time-of-flight aerosol mass spectrometry (HR-ToF-AMS, unpublished data) (*7*, *39*).

Table S1. Characteristics of the analyzed aerosol samples.

Sample Name	Sampling Time		Location	STXM setup
ATTO_2011_#1	2011/05/13	11:30-12:20	ATTO site	ALS, BESSY II
ATTO_2011_#2	2011/05/13	12:35-13:15	ATTO site	ALS
ATTO_2011_#7	2011/05/13	15:50-16:23	ATTO site	ALS
ATTO_2011_#8	2011/05/13	16:27-17:07	ATTO site	ALS
ATTO_2011_#9	2011/05/13	17:15-17:55	ATTO site	ALS, BESSY II
ATTO_2011_#10	2011/05/14	07:42-08:42	ATTO site	ALS
ZF2_2010_#3	2010/05/15	06:20-07:20	ZF2/TT34 site	ALS
ZF2_2010_#4	2010/05/15	08:46-09:46	ZF2/TT34 site	ALS
ZF2_2010_#5	2010/05/15	10:25:11:24	ZF2/TT34 site	ALS

Table S2. Experimental parameters for SOA generation in the Harvard Environmental Chamber (GMD = geometric mean diameter, GSD = geometric standard deviation).

VOC	Oxidation	Chamber RH [%]	Ammonium Sulfate Seeds		SOA	
			Dry Diameter [nm]	Concentration [μg m^{-3}]	Size Distribution GMD [nm] / GSD	Concentration [μg m^{-3}]
Isoprene	photooxidation (H_2O_2 injected, UV lights on)	40	70	2.4	152.4 / 1.44	32.7
α-pinene (+/-)	dark ozonolysis (O_3 injected, UV lights off)	40	46	1.0	94.2 / 1.58	26.1
β-caryophyllene	dark ozonolysis (O_3 injected, UV lights off)	40	46	0.5	95.1 / 1.65	18.2

Table S3. Resonance energies of the carbon K-edge NEXAFS features with corresponding functional groups and potassium L-edge transitions. Peak assignments are based on (*35, 38, 52, 103-104*).

Functionality	**Transition**	**Nominal Energy [eV]**
Alkene/aromatic, R(C*=C)R’	$1s \longrightarrow \pi^*$	285.0 ± 0.2
Carbonyl groups, R(C*=O)R’	$1s \longrightarrow \pi^*$	286.7 ± 0.2
Alkyl, C^*H_n (n=1,2,3)	$1s \longrightarrow \sigma^*_{C\text{-}H}$	287.7 ± 0.7
Carboxylic carbonyl, R(C*=O)OH	$1s \longrightarrow \pi^*$	288.7 ± 0.3
Hydroxy/ether, OC^*H_2	$1s \longrightarrow 3p/\sigma^*$	289.3 ± 0.2
Potassium, K_{L3}	$2p_{3/2} \longrightarrow 3d/\sigma^*$	297.4 ± 0.2
Potassium, K_{L2}	$2p_{1/2} \longrightarrow 3d/\sigma^*$	299.9 ± 0.2

Table S4. Molar elemental ratios for C, N, and O (n_O/n_C and n_N/n_C) for selected standard compounds, laboratory-generated SOA, and Amazonian OA determined by STXM-NEXAFS analysis. The reference data are stoichiometric ratios for pure standard compounds and AMS data for SOA samples. Data for BSA taken from Serro et al. (*105*). For SOA the ratios for organic plus ammonium sulfate and for organic only (in parentheses) are given.

Compound	**n_O/n_C**		**n_N/n_C**	
	STXM	**Reference**	**STXM**	**Reference**
Glucosamine·HCl ($C_6H_{14}NO_5Cl$)	0.86	0.83	0.17	0.17
Glucose ($C_6H_{12}O_6$)	0.90	1.0	0.04	0
Serine ($C_3H_7NO_3$)	0.75	1.0	0.28	0.33
Aspartic acid ($C_4H_7NO_4$)	1.0	1.0	0.23	0.25
BSA	0.36	0.32	0.17	0.25
Isoprene SOA	0.88 (0.63)	0.70 (0.67)	0.23	0.08 (0.004)
α-pinene SOA	0.42 (0.38)	0.36 (0.34)	0.06	0.04 (0.001)
β-caryophyllene SOA	0.35 (0.31)	0.33 (0.32)	0.04	0.02 (0.002)
OA_{acid}	0.63	-	0.09	-
OA_{mixed}	0.67	-	0.17	-
$OA_{hydroxyl}$	0.92	-	0.18	-

Table S5. WRF-ARW-v3.3.1 model configuration (*106*).

Scheme	Options
Microphysics	WRF Single-Moment 6-class scheme with ice, snow and graupel processes
Long-wave radiation	RRTMG scheme, a new version of RRTM
Short-wave radiation	RRTMG shortwave scheme with the MCICA method of random cloud overlap
Surface layer	Eta similarity used in Eta model and based on Monin-Obukhov with Zilitinkevich thermal roughness length and standard similarity functions from look-up tables
Land surface	Noah Land Surface Model unified NCEP/NCAR/AFWA scheme with soil temperature and moisture in four layers
Boundary layer	Mellor-Yamada-Janjic scheme, an Eta operational scheme; one-dimensional prognostic turbulent kinetic energy scheme with local vertical mixing
Cumulus parameterization	Grell 3D, an improved version of the GD scheme that may also be used on high resolution with subsidence spreading turned on
Diffusion	Full diffusion
6th order horizontal diffusion	Positive definite
Non-hydrostatic	True
PD advection	Positive definite on

Table S6. Normalized optical density at carbon absorption edge for reference and ambient aerosols as measured by STXM-NEXAFS and plotted against X-ray photon energy in Fig. 2A.

Energy [eV]	Normalized Optical Density						
	α-pinene SOA	*β*-caryophyllene SOA	isoprene SOA	glucose	OA(acid)	OA(mixed)	OA(hydroxy)
280	-0.03	0.02	0	0	0	-0.01	0
280.5	-0.03	0.02	0	-0.01	0	-0.01	0
281	-0.02	0.01	-0.01	-0.01	0	-0.02	0
281.5	-0.01	0	0	-0.01	0	-0.01	0
282	0	-0.01	0.01	-0.01	-0.01	-0.01	-0.01
282.5	0.01	0	0.01	-0.01	-0.01	-0.01	-0.01
283	0.03	0	0	-0.01	-0.01	-0.01	-0.01
283.1	0.03	0	0	-0.01	-0.01	-0.01	-0.01
283.2	0.02	0	0	-0.01	-0.01	-0.01	-0.01
283.3	0.01	0	0	-0.01	-0.01	0	-0.01
283.4	0.01	0	-0.01	-0.01	-0.01	0	-0.01
283.5	0	0.01	-0.01	-0.01	-0.01	0	-0.01
283.6	0.01	0.01	-0.01	0	0	0	-0.01
283.7	0.01	0	0	0	0	0.01	0
283.8	0.01	-0.01	0	0	0.01	0.01	0
283.9	0	-0.01	0.01	0	0.02	0.01	0
284	-0.01	-0.01	0.02	0.01	0.02	0.01	0.01
284.1	-0.01	-0.01	0.03	0.01	0.03	0.01	0.01
284.2	0	-0.01	0.04	0.01	0.03	0.01	0.01
284.3	0.01	-0.02	0.04	0.01	0.04	0.02	0.01
284.4	0.02	-0.01	0.05	0.02	0.06	0.04	0.01
284.5	0.03	0.03	0.06	0.02	0.07	0.05	0.02
284.6	0.04	0.06	0.06	0.02	0.09	0.07	0.02
284.7	0.06	0.1	0.07	0.03	0.12	0.09	0.02
284.8	0.08	0.12	0.07	0.03	0.14	0.11	0.03
284.9	0.1	0.13	0.08	0.04	0.17	0.14	0.03
285	0.11	0.14	0.08	0.05	0.19	0.16	0.03
285.1	0.11	0.14	0.08	0.06	0.21	0.19	0.03
285.2	0.1	0.14	0.08	0.06	0.22	0.2	0.03
285.3	0.1	0.13	0.09	0.06	0.22	0.21	0.03
285.4	0.11	0.13	0.09	0.06	0.21	0.2	0.03
285.5	0.11	0.12	0.09	0.05	0.2	0.19	0.03
285.6	0.12	0.11	0.1	0.05	0.18	0.18	0.03
285.7	0.12	0.1	0.1	0.04	0.17	0.16	0.03
285.8	0.13	0.09	0.11	0.04	0.15	0.15	0.03
285.9	0.14	0.1	0.12	0.05	0.15	0.14	0.03
286	0.16	0.11	0.14	0.06	0.15	0.13	0.04
286.1	0.19	0.12	0.16	0.07	0.16	0.14	0.05
286.2	0.22	0.15	0.19	0.09	0.18	0.15	0.06
286.3	0.27	0.2	0.22	0.11	0.21	0.17	0.08
286.4	0.33	0.28	0.26	0.13	0.25	0.2	0.09
286.5	0.41	0.4	0.3	0.15	0.28	0.24	0.11
286.6	0.47	0.52	0.34	0.16	0.31	0.27	0.12
286.7	0.51	0.61	0.37	0.17	0.34	0.29	0.12
286.8	0.52	0.65	0.4	0.17	0.35	0.3	0.12
286.9	0.53	0.67	0.41	0.16	0.36	0.31	0.11
287	0.53	0.67	0.43	0.16	0.36	0.32	0.11
287.1	0.54	0.68	0.44	0.16	0.36	0.34	0.12
287.2	0.57	0.71	0.47	0.16	0.37	0.36	0.13
287.3	0.62	0.76	0.5	0.17	0.38	0.38	0.14
287.4	0.68	0.83	0.55	0.19	0.4	0.41	0.16
287.5	0.74	0.92	0.6	0.2	0.43	0.45	0.17
287.6	0.82	1.01	0.66	0.22	0.47	0.49	0.2
287.7	0.9	1.11	0.74	0.24	0.54	0.55	0.23
287.8	1	1.22	0.83	0.27	0.63	0.64	0.28
287.9	1.12	1.33	0.93	0.33	0.75	0.76	0.35

288	1.27	1.44	1.06	0.4	0.9	0.9	0.44
288.1	1.46	1.58	1.21	0.48	1.05	1.06	0.55
288.2	1.73	1.74	1.38	0.57	1.22	1.21	0.67
288.3	2.07	1.96	1.58	0.65	1.39	1.35	0.8
288.4	2.48	2.2	1.78	0.73	1.55	1.47	0.94
288.5	2.87	2.42	1.99	0.82	1.68	1.56	1.07
288.6	3.12	2.56	2.16	0.92	1.76	1.62	1.2
288.7	3.18	2.57	2.3	1.04	1.77	1.63	1.32
288.8	3.05	2.48	2.4	1.19	1.73	1.62	1.44
288.9	2.79	2.33	2.46	1.36	1.65	1.6	1.56
289	2.51	2.17	2.5	1.54	1.57	1.59	1.68
289.1	2.27	2.04	2.52	1.7	1.49	1.58	1.8
289.2	2.08	1.95	2.52	1.82	1.43	1.58	1.9
289.3	1.95	1.89	2.53	1.9	1.38	1.58	1.95
289.4	1.87	1.85	2.53	1.93	1.36	1.59	1.96
289.5	1.82	1.83	2.53	1.92	1.33	1.58	1.93
289.6	1.8	1.83	2.52	1.88	1.31	1.56	1.88
289.7	1.8	1.83	2.51	1.82	1.3	1.54	1.82
289.8	1.81	1.83	2.5	1.76	1.29	1.51	1.75
289.9	1.81	1.83	2.48	1.7	1.28	1.48	1.68
290	1.82	1.83	2.46	1.65	1.29	1.45	1.63
290.1	1.82	1.84	2.44	1.6	1.29	1.44	1.59
290.2	1.83	1.84	2.43	1.57	1.3	1.44	1.57
290.3	1.83	1.86	2.41	1.56	1.31	1.45	1.58
290.4	1.83	1.87	2.4	1.57	1.33	1.47	1.6
290.5	1.81	1.88	2.38	1.59	1.35	1.49	1.64
290.6	1.8	1.89	2.36	1.61	1.36	1.51	1.68
290.7	1.8	1.9	2.35	1.64	1.37	1.53	1.71
290.8	1.81	1.92	2.34	1.65	1.38	1.55	1.74
290.9	1.82	1.92	2.32	1.66	1.38	1.56	1.74
291	1.82	1.92	2.31	1.66	1.38	1.56	1.74
291.1	1.81	1.93	2.31	1.64	1.37	1.57	1.72
291.2	1.81	1.94	2.3	1.63	1.37	1.57	1.69
291.3	1.83	1.95	2.3	1.62	1.37	1.56	1.67
291.4	1.84	1.96	2.3	1.6	1.37	1.56	1.66
291.5	1.85	1.96	2.29	1.6	1.38	1.56	1.66
291.6	1.85	1.96	2.3	1.59	1.4	1.56	1.66
291.7	1.84	1.97	2.3	1.59	1.41	1.56	1.66
291.8	1.85	1.98	2.3	1.59	1.42	1.57	1.66
291.9	1.87	1.99	2.3	1.6	1.42	1.57	1.66
292	1.88	2.01	2.31	1.6	1.41	1.57	1.67
292.1	1.89	2.02	2.31	1.61	1.41	1.57	1.68
292.2	1.9	2.02	2.32	1.63	1.41	1.58	1.7
292.3	1.91	2.01	2.32	1.64	1.42	1.59	1.71
292.4	1.91	2.01	2.32	1.64	1.43	1.6	1.73
292.5	1.92	2	2.32	1.65	1.44	1.61	1.74
292.6	1.92	2.01	2.32	1.65	1.45	1.62	1.76
292.7	1.91	2.01	2.32	1.65	1.45	1.63	1.77
292.8	1.91	2	2.31	1.65	1.45	1.63	1.77
292.9	1.89	2	2.31	1.65	1.45	1.63	1.77
293	1.88	1.99	2.31	1.66	1.45	1.63	1.78
293.1	1.87	1.99	2.3	1.66	1.46	1.64	1.79
293.2	1.86	1.99	2.3	1.66	1.47	1.64	1.79
293.3	1.86	1.97	2.29	1.65	1.46	1.65	1.8
293.4	1.86	1.96	2.29	1.64	1.46	1.65	1.79
293.5	1.86	1.96	2.28	1.64	1.46	1.65	1.78
293.6	1.87	1.96	2.28	1.63	1.46	1.65	1.77
293.7	1.87	1.97	2.27	1.63	1.47	1.65	1.77
293.8	1.87	1.97	2.26	1.62	1.47	1.65	1.77
293.9	1.87	1.96	2.26	1.62	1.46	1.65	1.76
294	1.87	1.93	2.25	1.61	1.45	1.64	1.74
294.5	1.86	1.89	2.21	1.6	1.45	1.63	1.72

294.721	1.85	1.88	2.19	1.59	1.46	1.63	1.7
294.942	1.85	1.86	2.17	1.58	1.47	1.62	1.68
295.163	1.84	1.85	2.14	1.57	1.49	1.62	1.66
295.384	1.83	1.83	2.12	1.55	1.5	1.62	1.65
295.605	1.82	1.82	2.09	1.54	1.53	1.61	1.64
295.826	1.81	1.8	2.07	1.52	1.56	1.62	1.64
296.047	1.8	1.79	2.05	1.5	1.61	1.64	1.64
296.268	1.78	1.77	2.03	1.49	1.67	1.68	1.65
296.489	1.77	1.76	2.01	1.47	1.75	1.73	1.68
296.71	1.75	1.75	1.99	1.45	1.83	1.79	1.71
296.931	1.74	1.73	1.97	1.44	1.92	1.85	1.76
297.152	1.72	1.72	1.95	1.42	1.97	1.9	1.78
297.373	1.7	1.71	1.92	1.4	1.97	1.89	1.77
297.594	1.69	1.7	1.9	1.38	1.9	1.84	1.72
297.815	1.67	1.69	1.88	1.37	1.79	1.76	1.65
298.036	1.66	1.67	1.85	1.35	1.68	1.67	1.59
298.257	1.64	1.66	1.83	1.34	1.61	1.61	1.54
298.478	1.63	1.64	1.81	1.33	1.57	1.57	1.51
298.699	1.61	1.62	1.79	1.32	1.57	1.57	1.5
298.92	1.6	1.6	1.77	1.3	1.6	1.59	1.52
299.141	1.57	1.58	1.76	1.29	1.67	1.63	1.55
299.362	1.55	1.57	1.74	1.28	1.76	1.69	1.59
299.583	1.53	1.55	1.73	1.26	1.85	1.74	1.62
299.804	1.52	1.53	1.71	1.25	1.9	1.77	1.63
300.025	1.52	1.51	1.7	1.22	1.91	1.76	1.61
300.246	1.51	1.5	1.68	1.2	1.85	1.71	1.56
300.467	1.5	1.48	1.66	1.18	1.75	1.64	1.5
300.688	1.49	1.47	1.64	1.18	1.65	1.57	1.44
300.909	1.48	1.46	1.61	1.19	1.57	1.51	1.39
301.13	1.46	1.45	1.58	1.19	1.51	1.47	1.36
301.351	1.45	1.44	1.57	1.19	1.47	1.45	1.33
301.572	1.44	1.43	1.55	1.18	1.45	1.43	1.31
301.793	1.43	1.42	1.53	1.18	1.42	1.42	1.29
302.014	1.42	1.41	1.52	1.17	1.4	1.4	1.28
302.235	1.41	1.4	1.5	1.17	1.38	1.39	1.28
302.456	1.4	1.38	1.49	1.16	1.36	1.38	1.27
302.677	1.38	1.37	1.48	1.16	1.34	1.36	1.27
302.898	1.37	1.36	1.47	1.16	1.33	1.35	1.26
303.119	1.36	1.35	1.46	1.16	1.33	1.34	1.25
303.34	1.35	1.34	1.45	1.16	1.33	1.32	1.24
303.561	1.34	1.33	1.44	1.15	1.32	1.3	1.22
303.782	1.33	1.32	1.43	1.15	1.28	1.27	1.2
304.003	1.32	1.31	1.41	1.13	1.23	1.22	1.16
305	1.27	1.26	1.36	1.09	1.15	1.15	1.1
310	1.09	1.08	1.08	1.03	1.06	1.06	1.03
315	0.91	0.91	0.92	0.97	0.96	0.96	0.96

Table S7. Normalized optical density at carbon absorption edge for Amazonian aerosol particles with different potassium contents as measured by STXM-NEXAFS and plotted against X-ray photon energy in Fig. 2B.

Energy [eV]	Normalized Optical Density		
	OA with high K mass fraction (>10%)	OA with medium K mass fraction (1-10%)	OA with low K mass fraction (<1%)
280	0.03	0.02	-0.01
280.5	0.03	0.01	-0.01
281	0.03	0	-0.01
281.5	0.03	0	-0.01
282	0.04	0	-0.01
282.5	0.03	0	-0.02
283	0.03	0	-0.02
283.1	0.02	-0.01	-0.02
283.2	0.02	-0.02	-0.01
283.3	0	-0.03	-0.01
283.4	-0.01	-0.04	0
283.5	-0.02	-0.04	0
283.6	-0.04	-0.05	0
283.7	-0.05	-0.05	0.01
283.8	-0.05	-0.04	0.01
283.9	-0.05	-0.03	0.02
284	-0.05	-0.02	0.02
284.1	-0.05	-0.01	0.02
284.2	-0.06	0.01	0.03
284.3	-0.07	0.02	0.04
284.4	-0.09	0.03	0.05
284.5	-0.12	0.05	0.07
284.6	-0.16	0.06	0.09
284.7	-0.21	0.08	0.11
284.8	-0.25	0.09	0.12
284.9	-0.28	0.11	0.14
285	-0.29	0.12	0.16
285.1	-0.27	0.13	0.18
285.2	-0.24	0.14	0.19
285.3	-0.2	0.14	0.19
285.4	-0.16	0.13	0.18
285.5	-0.13	0.12	0.18
285.6	-0.12	0.12	0.16
285.7	-0.13	0.11	0.15
285.8	-0.17	0.11	0.14
285.9	-0.22	0.12	0.13
286	-0.26	0.13	0.13
286.1	-0.3	0.14	0.14
286.2	-0.31	0.16	0.15
286.3	-0.31	0.19	0.17
286.4	-0.3	0.21	0.19
286.5	-0.26	0.24	0.22
286.6	-0.22	0.25	0.24
286.7	-0.16	0.26	0.26
286.8	-0.12	0.27	0.28
286.9	-0.1	0.27	0.3
287	-0.1	0.27	0.31
287.1	-0.12	0.27	0.33
287.2	-0.13	0.29	0.35
287.3	-0.13	0.31	0.37
287.4	-0.11	0.34	0.4
287.5	-0.08	0.37	0.44
287.6	-0.03	0.42	0.48
287.7	0.03	0.48	0.55
287.8	0.1	0.56	0.64
287.9	0.18	0.65	0.75
288	0.26	0.75	0.88

288.1	0.35	0.86	1.02
288.2	0.43	0.98	1.16
288.3	0.52	1.1	1.3
288.4	0.6	1.22	1.41
288.5	0.66	1.32	1.51
288.6	0.7	1.4	1.59
288.7	0.73	1.45	1.64
288.8	0.73	1.49	1.67
288.9	0.71	1.5	1.69
289	0.68	1.5	1.7
289.1	0.64	1.49	1.71
289.2	0.6	1.48	1.72
289.3	0.55	1.48	1.72
289.4	0.5	1.47	1.72
289.5	0.47	1.46	1.7
289.6	0.45	1.44	1.68
289.7	0.45	1.42	1.65
289.8	0.46	1.4	1.62
289.9	0.47	1.37	1.59
290	0.48	1.34	1.57
290.1	0.48	1.32	1.56
290.2	0.48	1.31	1.55
290.3	0.5	1.31	1.56
290.4	0.53	1.33	1.57
290.5	0.57	1.36	1.59
290.6	0.6	1.4	1.62
290.7	0.62	1.43	1.63
290.8	0.61	1.45	1.65
290.9	0.58	1.46	1.65
291	0.53	1.45	1.66
291.1	0.47	1.45	1.66
291.2	0.41	1.44	1.65
291.3	0.35	1.44	1.65
291.4	0.32	1.44	1.65
291.5	0.3	1.44	1.65
291.6	0.3	1.44	1.66
291.7	0.31	1.44	1.66
291.8	0.33	1.44	1.66
291.9	0.34	1.43	1.66
292	0.35	1.43	1.67
292.1	0.36	1.43	1.67
292.2	0.36	1.44	1.68
292.3	0.36	1.46	1.69
292.4	0.34	1.48	1.7
292.5	0.32	1.49	1.71
292.6	0.29	1.5	1.72
292.7	0.26	1.5	1.73
292.8	0.22	1.49	1.74
292.9	0.19	1.48	1.74
293	0.17	1.48	1.75
293.1	0.16	1.48	1.75
293.2	0.16	1.48	1.76
293.3	0.17	1.48	1.76
293.4	0.19	1.49	1.76
293.5	0.19	1.5	1.76
293.6	0.18	1.5	1.76
293.7	0.16	1.5	1.75
293.8	0.13	1.5	1.75
293.9	0.13	1.5	1.74
294	0.14	1.49	1.73
294.5	0.18	1.48	1.72
294.721	0.23	1.48	1.71
294.942	0.3	1.48	1.7
295.163	0.4	1.49	1.7
295.384	0.55	1.51	1.7
295.605	0.77	1.55	1.7

295.826	1.06	1.61	1.71
296.047	1.41	1.7	1.72
296.268	1.83	1.79	1.74
296.489	2.31	1.9	1.76
296.71	2.8	2	1.79
296.931	3.2	2.08	1.8
297.152	3.39	2.11	1.81
297.373	3.28	2.09	1.8
297.594	2.88	2.01	1.76
297.815	2.33	1.89	1.72
298.036	1.8	1.78	1.67
298.257	1.46	1.69	1.63
298.478	1.36	1.65	1.6
298.699	1.49	1.66	1.59
298.92	1.79	1.71	1.59
299.141	2.2	1.78	1.61
299.362	2.63	1.87	1.64
299.583	2.99	1.93	1.66
299.804	3.21	1.96	1.67
300.025	3.23	1.95	1.66
300.246	3.05	1.89	1.63
300.467	2.76	1.79	1.59
300.688	2.43	1.69	1.55
300.909	2.16	1.6	1.5
301.13	1.95	1.53	1.46
301.351	1.79	1.48	1.43
301.572	1.67	1.45	1.41
301.793	1.56	1.42	1.39
302.014	1.45	1.41	1.37
302.235	1.35	1.4	1.36
302.456	1.26	1.39	1.35
302.677	1.19	1.38	1.34
302.898	1.13	1.37	1.32
303.119	1.08	1.35	1.31
303.34	1.06	1.32	1.3
303.561	1.05	1.28	1.27
303.782	1.06	1.24	1.24
304.003	1.05	1.19	1.19
305	1.03	1.12	1.13
310	0.97	1.05	1.05
315	0.9	0.98	0.97

Table S8. Potassium mass fraction for OA particles from ZF2-samples (Sect. S1.1) as plotted against particle volume equivalent diameter (D_{ve}) in Fig. 3.

	D_{ve} [µm]	Potassium Mass Fraction [%]
OA(acid)	0.40	16.3
	0.36	9.1
	0.30	8.5
	0.55	7.7
	0.36	7.2
	0.42	6.4
	0.57	5.2
	0.41	4.9
	0.39	4.5
	0.30	4.5
	0.34	4.2
	0.25	3.5
	0.45	2.8
	0.39	2.0
	0.41	1.7
	0.58	1.6
	0.91	1.6
	0.38	0.5
	1.06	0.4
	0.34	0.0
OA(mixed)	0.50	7.0
	0.37	3.9
	0.45	2.7
	0.35	0.0
	0.35	0.0

Table S9. Potassium mass fraction for OA particles from ATTO-samples (Sect. S1.1) as plotted against particle volume equivalent diameter (D_{ve}) in Fig. 3.

	D_{ve} [µm]	Potassium Mass Fraction [%]
OA(acid)	0.35	5.2
	0.88	4.1
	0.43	3.4
	0.51	3.2
	0.27	3.0
	0.52	2.7
	0.41	2.6
	0.61	2.2
	0.67	1.5
	0.62	1.5
	1.07	0.6
	0.96	0.4
OA(mixed)	0.61	6.0
	0.30	4.5
	0.38	4.2
	0.48	3.7
	0.34	3.3
	0.59	3.3
	0.19	3.2
	0.48	2.7
	0.56	2.4
	0.48	2.2
	0.44	1.9
	0.43	1.6
	0.51	1.2
	0.80	1.2
	0.63	1.2
	0.74	1.1
	0.58	1.0
	1.02	1.0
	0.47	0.9
	0.62	0.8
	0.70	0.7
	0.41	0.6
	0.76	0.6
	0.87	0.6
	0.69	0.5
	0.90	0.5
	0.65	0.5
	0.93	0.3

OA(hydroxy)	0.33	10.6
	0.38	6.1
	0.54	2.6
	0.62	2.3
	0.74	2.0
	0.52	1.6
	0.80	1.4
	0.70	1.0
	0.99	1.0
	1.01	0.9
	0.75	0.8
	0.93	0.3
Salts + OA	0.20	19.8
	0.16	19.5
	0.12	18.8
	0.17	13.3
	0.26	12.4
	0.17	12.4
	0.37	8.5
	0.30	5.0
	0.34	3.5